CORRECTED 9 JULY 2026; SEE LAST PAGE

Check for updates

RESEARCH ARTICLE SUMMARY

ICE SHEETS

# Continental breakup-driven uplift instigated East Antarctic Ice Sheet formation

Thomas M. Gernon*†, Thea K. Hincks†, Philip Goodwin, Guy J. G. Paxman, Sascha Brune, Eelco J. Rohling, Derek Keir, Jean Braun

Full article and list of author affiliations: https://doi.org/10.1126/science.adz6758

**INTRODUCTION:** The East Antarctic Ice Sheet (EAIS) is Earth's oldest and largest ice mass, sequestering the equivalent of ~52 m of global sea level, but its formation is poorly understood. A long-standing enigma is how the EAIS emerged at the Eocene-Oligocene Transition [EOT, ~34 million years ago (Ma)] under relatively warm global climates that persisted well into the Oligocene (ending ~23 Ma). If declining atmospheric $CO_2$ were the sole driver, then a synchronous global cooling would be expected in both hemispheres. Instead, Northern Hemisphere glaciation lagged Antarctica by 20 to 25 million years (Myr). This suggests that a key process governing EAIS initiation is missing from climate–ice sheet models.

**RATIONALE:** Earlier studies suggest that glaciation in Eastern Antarctica began as regional ice caps centred on the Transantarctic, Gamburtsev, and Dronning Maud Land (DML) mountains. These then expanded and coalesced at the EOT to form the EAIS. We hypothesize that geodynamic surface uplift, causally related to continental breakup between Africa and Antarctica more than 100 Myr earlier, preconditioned Antarctica for ice sheet expansion. We tested this by combining landscape evolution models with energy balance and ice sheet models to isolate the climatic impact of evolving topography over multimillion-year timescales. We assessed elevation thresholds for ice sheet growth under a range of plausible global temperature states and evaluated how different uplift scenarios may have influenced global mean surface temperatures.

**RESULTS:** Landscape evolution modeling shows that continental breakup generated a >2-km-high coastal escarpment in DML and an elevated plateau extending ~2000 km inland. The resulting wave of uplift and exhumation migrated inland, taking ~100 Myr to reach the ancestral Gamburtsev Mountains. Renewed uplift (rejuvenation) of the Gamburtsevs in the Eocene resulted in a fluvially incised mountain landscape, later locally overprinted by alpine-style glaciation. Uplift in the ~15 Myr preceding the EOT greatly expanded the area above the permanent snow line. Together, our ice sheet and energy balance models indicate that dynamic uplift controlled the timing of ice cap expansion, pushing elevations above the threshold for ice sheet growth at ~45 Ma. This uplift enabled EAIS formation under relatively warm climatic conditions and stimulated ~1.0°C of global cooling through albedo feedback. That level of global cooling remained insufficient to trigger glaciation on (lower-elevation) Northern Hemisphere landmasses.

**CONCLUSION:** Multimillion-year uplift can account for enigmatic aspects of the Antarctic landscape, including the alpine-scale relief of the Gamburtsev Mountains. Crucially, multimillion-year topographic evolution creates shifting thresholds for glaciation that are not captured by existing global climate models. Regional uplift and associated local cooling of the land surface facilitates ice sheet development under relatively warm global conditions, reconciling Oligocene polar warmth with the onset of the icehouse world. The interplay of declining global temperatures and surface uplift in East Antarctica can explain the earlier onset of Southern Hemisphere ice sheets relative to those in the Northern Hemisphere. This system of landscape–ice sheet–climate coevolution represents a powerful driver of glaciation that may also have affected earlier ice ages. □

*Corresponding author. Email: t.m.gernon@soton.ac.uk †These authors contributed equally to this work. Cite this article as T. M. Gernon *et al.*, *Science* 393, eadz6758. DOI: 10.1126/science.adz6758

Downloaded from https://www.science.org at University of Southampton on October 15, 2026

**Sensitivity of ice sheet nucleation to evolving topography in East Antarctica.** Ice sheet models using reconstructed topographies under fixed climatic conditions reveal sensitivity of ice sheets to changing topography, with uplift driving their expansion and stabilization in the Gamburtsev Mountains by 34 Ma.

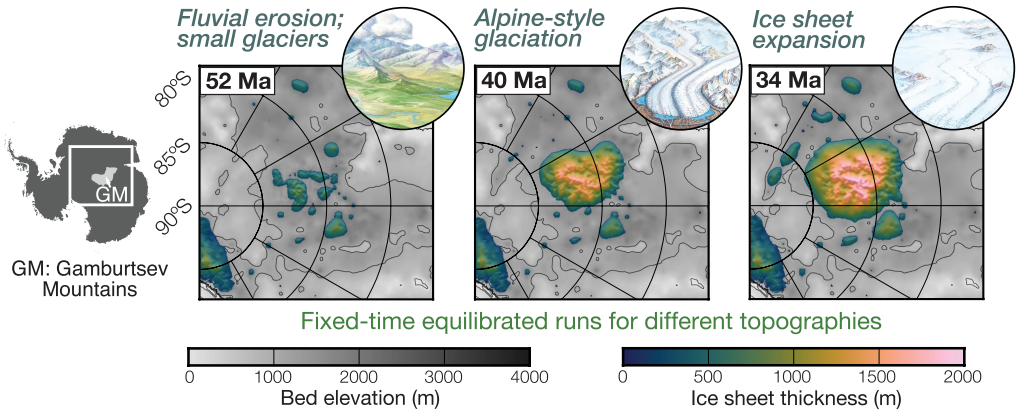


ILLUSTRATIONS: GARY HINCKS.

ICE SHEETS

# Continental breakup-driven uplift instigated East Antarctic Ice Sheet formation

Thomas M. Gernon[1,2]*†, Thea K. Hincks[1]†, Philip Goodwin[1], Guy J. G. Paxman[3], Sascha Brune[2,4], Eelco J. Rohling[1,5], Derek Keir[1,6], Jean Braun[2,4]

Why Antarctica became glaciated ~34 million years ago (Ma) remains debated, as relatively warm climates and sea temperatures appear inconsistent with ice sheet formation. Although a critical decline in $CO_2$ is considered primarily responsible, evidence suggests that other factors were important, too. We investigated whether regional topographic uplift, rooted in Jurassic continental breakup and mantle-surface feedbacks, enabled nucleation of the East Antarctic Ice Sheet (EAIS). By integrating geodynamic-topographic models with ice sheet and energy balance models, we show that progressive plateau growth in East Antarctica, including Eocene uplift of the Gamburtsev Mountains, pushed landscapes above the threshold for ice sheet nucleation by ~45 Ma. Uplift enabled EAIS growth under warmer-than-expected climates, producing hemispheric asymmetry in early glaciation and reconciling Oligocene polar warmth with the onset of the modern icehouse world.

The East Antarctic Ice Sheet (EAIS) is Earth's oldest and largest ice mass, with a sea-level equivalent of 52 m ($m_{seq}$, meaning global mean sea level would rise 52 m if the EAIS melted) (*1*, *2*). The EAIS formed after 15 million years (Myr) of global cooling (*3*) and culminated in major ice sheet expansion at the Eocene-Oligocene Transition [EOT; 34.4 to 33.7 million years ago (Ma)] (Fig. 1, A and B). Ice sheet initiation is widely attributed to a decline in atmospheric $CO_2$ below a critical threshold of ~600 parts per million, triggering global cooling and glaciation (*4*, *5*). Yet, if $CO_2$ forcing alone drove this glaciation, then a broad, synchronous cooling affecting both hemispheres should be evident. Instead, Northern Hemisphere glaciation lagged by >20 Myr (*6*), $TEX_{86}$-based sea-surface temperature (SST) records indicate unexpectedly warm Southern Ocean conditions for ~10 Myr following the EOT (*7*), and $\delta^{18}O$-based records show limited global cooling persisting well into the Oligocene (*8*), all seemingly at odds with continental glaciation. This paradox raises a fundamental question: How did the EAIS form?

EAIS formation likely involved a confluence of events, including $CO_2$ forcing (*4*, *5*), perhaps tied to Himalayan mountain uplift (*9*) and/or changes in mantle $CO_2$ degassing and paleogeography (*10*). One underexplored factor is the role of uplifting continental plateaus in polar regions, such as Antarctica, where reduced insolation is expected to amplify the cooling effects of surface uplift on early ice dynamics. Surface temperatures generally decrease with elevation through direct lapse rate and subsequent cryosphere-albedo feedback, with both uplift (*11*) and high terrain (*12*) promoting ice sheet growth and stability. The EAIS likely originated as dynamic, ~1000-km-wide ice caps centered on the highlands of Dronning Maud Land (DML), the Gamburtsev Mountains, and the Transantarctic Mountains (*4*). In the Transantarctic Mountains, stepwise uplift and glaciation are evident (Fig. 1C), with mountain glaciers present up to 20 Myr before full EAIS expansion at the EOT (*13*, *14*).

Relevant to Antarctica, it has recently been shown that continental breakup exerts a geodynamic legacy on cratonic interiors, including plateau uplift, lasting tens to more than a hundred million years (*15*, *16*). Specifically, continental rifting can initiate a wave of mantle instabilities that migrate progressively toward cratonic interiors, the ancient cores of continents (*15*). This process induces surface uplift through convective removal and lithospheric thinning, dynamically reorganizing topography in space and time (*16*). These rift-related processes combine to create steep coastal escarpments and high elevation plateaus (*16*), features that also dominate the East Antarctic landscape (Fig. 1D and fig. S1). This suggests a mechanistic link between ancient breakup events (e.g., fig. S2), multimillion-year landscape evolution, and continental glaciation.

We investigated whether this long-term landscape evolution affected EAIS formation at its primary nucleation sites (*4*). Recent Earth System Model (ESM) simulations provide "snapshot" insights into the atmospheric and oceanic thresholds required for Antarctic ice sheet nucleation (*17*), with some efforts informed by diverse observational constraints (*13*). These studies typically utilize static paleotopographic reconstructions [e.g., (*18*)] to test climate sensitivity at discrete time slices, such as the Early Oligocene Glacial Maximum (*13*). Our approach instead treats the solid Earth and surface environment as dynamic, interacting, time-dependent components. Rather than reconstructing a static "true" ice sheet configuration for the early Oligocene (*13*, *17*), we coupled geodynamic-topographic evolution with ice sheet and energy balance models to explore the multimillion-year sensitivity of ice cover to progressive uplift, a geologic forcing seldom considered in climate models. This approach allowed us to examine the coevolution of topography and climate during the long descent into continental glaciation, thus providing new context to the transition itself (Fig. 1, A and B).

Our focus is on the DML escarpment and the Gamburtsev Mountains (Fig. 1D). In DML, a laterally extensive, kilometer-high escarpment rims the continental margin and originated during continental rifting and Africa-Antarctica breakup in the Jurassic (*16*, *19*) (fig. S2). The Gamburtsev Mountains are an enigmatic intraplate mountain range within a stable craton (*20*–*23*). Unusually for a craton, these mountains show evidence of relatively recent uplift, likely in the millions of years prior to EAIS glaciation, as indicated by preserved alpine-style geomorphology featuring 2 to 3 km of relief beneath the dry-based, slow-moving ice sheet (*21*). We examine the role of geodynamically-forced uplift in explaining this enigmatic relief and its implications for stimulating EAIS nucleation. We further investigate whether and how evolving topography generates shifting thresholds for glaciation, an effect not captured by static climate models.

## Results

### Uplift occurred during EAIS glaciation

To evaluate the onset and extent of EAIS glaciation, we formulated a probabilistic version of an ice sheet parameterization (*6*, *24*) that incorporates glacial isostatic adjustment, bed slope, and evolving basal friction (see Materials and methods). The model allows dynamic ice sheet aspect ratios linked to regolith development and topographic feedbacks and applies Monte Carlo sampling to the $\delta^{18}O$–sea level relationship across its full uncertainty range. This approach yields an uncertainty-resolved reconstruction of Antarctic ice sheet growth, bedrock response, and spatial extent through time. The model suggests low-profile Antarctic ice at total volumes of ~5 $m_{seq}$ from as early as ~47 Ma, increasing to up to ~15 $m_{seq}$ from ~40 Ma (Fig. 1B). This protracted glacial onset is consistent with geologic records (*14*, *25*, *26*) and climate models (*17*, *27*). Indeed, simulations by (*17*) suggest that substantial ice volumes persisted in Antarctica well before the EOT without a continent-wide glaciation, consistent with Klages *et al.* (*13*),

[1]School of Ocean & Earth Science, University of Southampton, Southampton, UK. [2]GFZ Helmholtz Centre for Geosciences, Telegrafenberg, Potsdam, Germany. [3]Department of Geography, Durham University, Durham, UK. [4]Institute of Geosciences, University of Potsdam, Potsdam-Golm, Germany. [5]Department of Earth Sciences, Utrecht University, Utrecht, Netherlands. [6]Department of Earth Sciences, Università degli Studi di Firenze, Florence, Italy. ***Corresponding author. Email: t.m.gernon@soton.ac.uk** †These authors contributed equally to this work.

Downloaded from https://www.science.org at University of Southampton on October 15, 2026

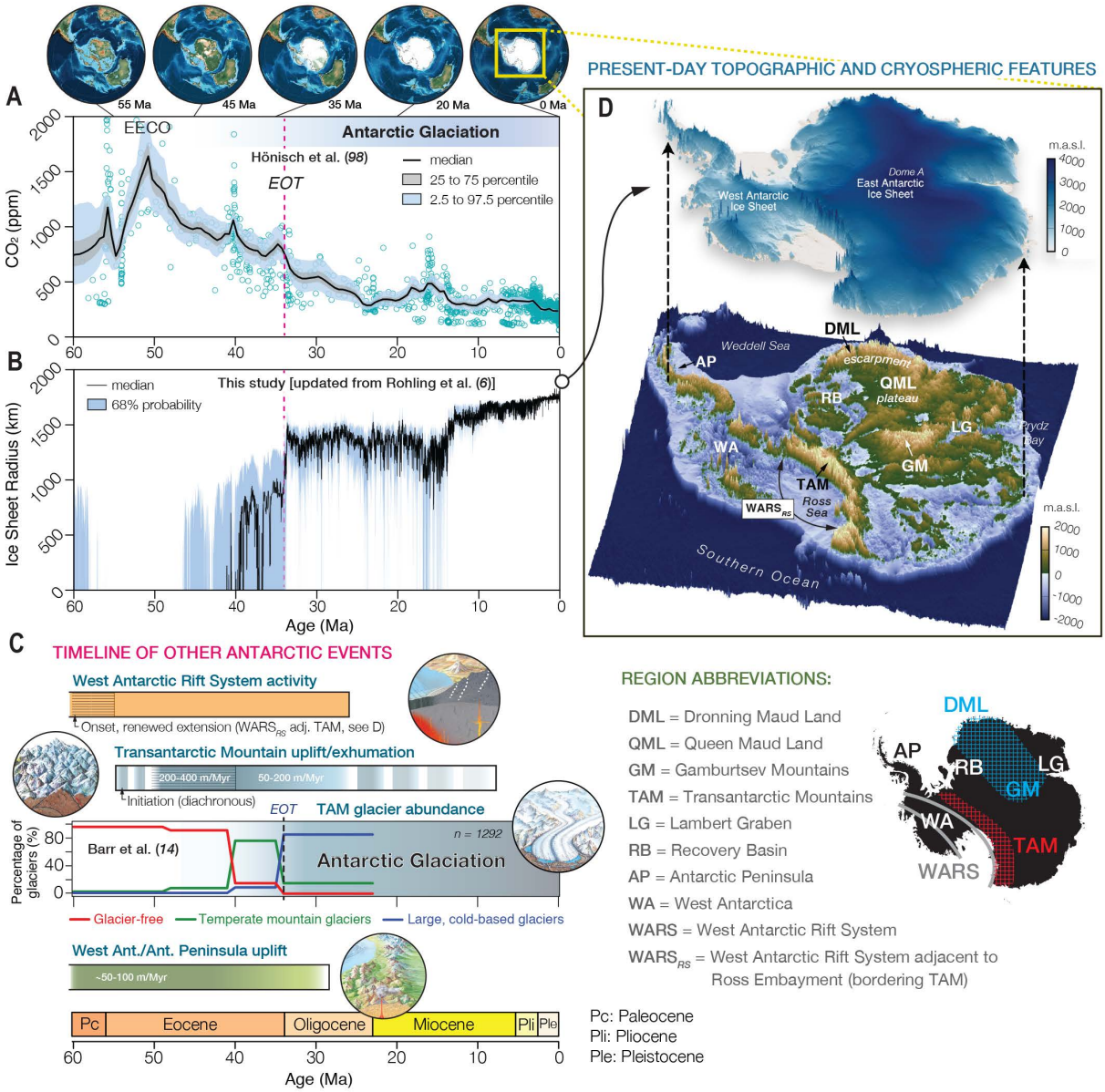


**Fig. 1. Descent into the Antarctic icehouse.** (**A**) Atmospheric $CO_2$ concentrations during the Cenozoic [data from (*98*)], showing a long-term decline from the Early Eocene Climatic Optimum (EECO, ~53 to 49 Ma) and marked drop at the EOT; paleogeographic reconstructions are from (*99*). ppm, parts per million. (**B**) Modeled ice sheet radius in Antarctica through time; early ice sheets were widespread but low profile (potentially as early as ~47 Ma), with radii reaching ~1000 km from ~40 Ma; analysis updated from (*6*,*24*) (see Materials and methods). (**C**) Timeline of Antarctic uplift and tectonic events [inset images from (*100*)], with uplift ages from (*34*–*37*) (supplementary text) and glacier abundance from (*14*). Crustal extension in the WARS commenced at 105 to 85 Ma, with renewed extension in the Ross Sea region ($WARS_{RS}$) during the Cenozoic (*37*,*39*). (**D**) Shown for context is the present-day bed topography of Antarctica, from BedMachine compilations (*1*), with relevant physiographic features labeled (see key); figure modified from https://s-ink.org/antarctica-topography. m.a.s.l., meters above sea level.

who inferred that West Antarctica was ice sheet free in the early Oligocene.

Notably, the onset of full glaciation at the EOT (Fig. 1B) coincides with the culmination of documented uplift events across Antarctica (Fig. 1C; supplementary text). We propose that preglacial uplift in Antarctica was more widespread than previously recognized. Specifically, we argue that both the DML escarpment and Gamburtsev Mountains arose directly from the continental breakup of Africa-Antarctica, reflecting mantle-surface feedbacks that persisted for >120 Myr. We further propose that the Gamburtsev Mountains experienced renewed uplift (i.e., rejuvenation) in the Eocene (56 to 33.9 Ma), raising the possibility that it promoted ice cap coalescence in the Late Eocene (*4*), seeding the incipient EAIS. Between the DML escarpment and Gamburtsev Mountains, the Queen Maud Land (QML) region constitutes a ~1.25-km-high plateau flanked by highlands (Fig. 1D and fig. S1), a configuration closely resembling the Central Plateau of South Africa, which was tectonically connected to this region within Gondwana (fig. S2) and underwent analogous escarpment and plateau uplift processes (*16*).

## Continental rifting drove Antarctic landscape evolution and uplift

To evaluate how evolving topography may have influenced EAIS formation, we simulated geomorphic changes through time using a landscape evolution model (Fig. 2; see Materials and methods). The landscape model solves the stream power law and hillslope diffusion equations for time- and space-dependent uplift (*16*, *28*), which are sufficient to

Downloaded from https://www.science.org at University of Southampton on October 15, 2026

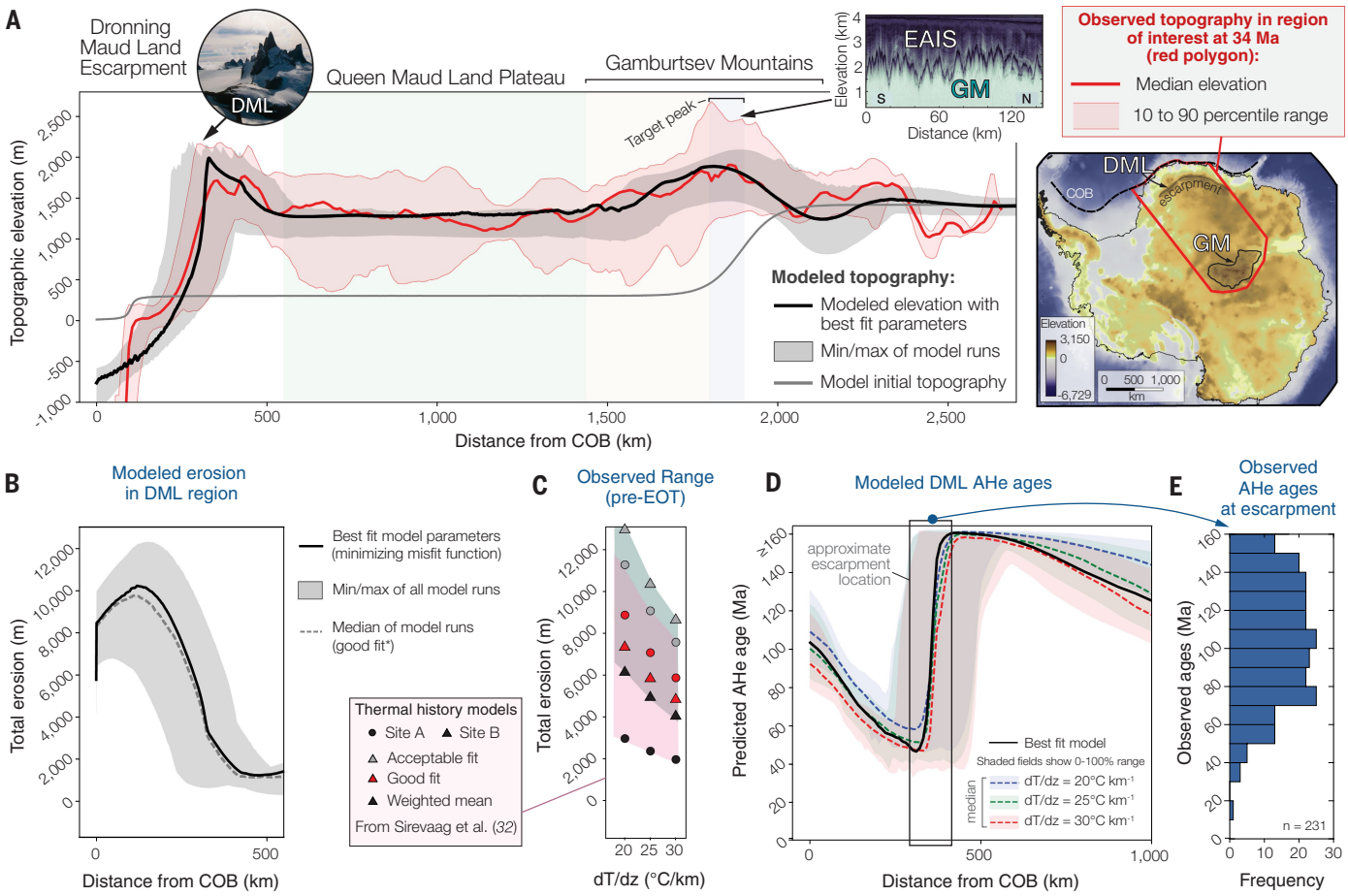


**Fig. 2. Simulated long-term uplifts in Antarctica following continental breakup.** (**A**) Modeled topographic profile (black line) after 126 Myr of landscape evolution (from 160 to 34 Ma) compared with the observed topography across a swath of the region (red polygon in inset shows swath location). This distance is measured from the continent-ocean boundary (COB). A full range of observed topographies and model runs, incorporating uncertainties, are shown; the inset image depicting a radar echogram from the Gamburtsevs is adapted from (*22*). For model evolution at individual time steps, see fig. S4A. (**B**) Modeled total erosion across the DML escarpment, calculated using the preferred model with best-fit parameters (minimizing the misfit function). Model runs yielding a misfit value ≤0.7 are considered "good fits." The full erosion profile is given in fig. S4B. (**C**) Total erosion (pre-EOT, ~180 to 34 Ma) estimated from thermal history models of two DML sites, showing acceptable and good fits, as well as weighted mean models [data from (*32*)]; results shown for three different geothermal gradients; note that the total erosion is comparable with modeled results shown in (B). (**D**) Modeled AHe thermochronological ages for the DML escarpment, shown for three geothermal gradients to capture probable uncertainty. The full profile, along with predicted apatite fission track (AFT) ages, is shown in fig. S5. (**E**) Measured AHe ages ≤160 Ma from the same DML region for direct comparison, with model predictions in (D) [$n$ = 231 age observations; data from (*32*)]; all samples (including ≥160 Ma) are shown in fig. S6. Note the similarity between modeled and observed youngest AHe ages in areas of rock exposure.

capture topographic evolution prior to glaciation (see Materials and methods). The model is constrained by plate kinematic reconstructions (*19*), geodynamic models (*16*) and geologic observations (see Materials and methods and supplementary text). Further, our modeling strategy incorporates known ranges of Antarctic crustal properties, including effective elastic thickness ($T_e$; fig. S3), geothermal gradient, and rift timing. It is further refined by identifying parameter combinations (see Materials and methods) that successfully reproduce the spatial variation in topography at 34 Ma (*18*).

To match the scale of Antarctic physiography in the study region (Fig. 2A), we limited the horizontal extent of the analysis to 2500 km (see Materials and methods). We defined an initial topography that includes an expansive, low-relief region along with modest highlands in the Gamburtsevs, which were purportedly formed by rift-flank flexural uplift along the Lambert Graben between ~250 and 100 Ma (*29*) (though older origins have also been proposed; see Materials and methods). Indeed, our landscape models best reproduce observed topography when they incorporate a localized, 500-km-wide preexisting high (1300 to 1500 m elevation), adjacent to the Lambert Graben (Fig. 2A). Nevertheless, both the reniform, non–rift-parallel morphology of the Gamburtsev Mountains and the detrital thermochronology from Prydz Bay (*30*) suggest that their origin cannot be fully explained by ancient, proximal rift-related processes. It is thus feasible that an older, modest topographic high was rejuvenated by a delayed mantle-driven wave of uplift in the Eocene, explaining the elevated, seemingly youthful relief of the Gamburtsevs (*21*).

Our reference landscape model (Fig. 2A) provides the best fit to the overall Antarctic topography, as characterized by the location and median elevation of the DML escarpment and Gamburtsev Mountains at 34 Ma (tables S1 to S3). The landscape model revealed stepwise plateau growth over time (Fig. 2A, figs. S4 and S5, and movie S1), driven by a wave of erosion resulting from isostatic uplift related to dynamic mantle effects [as shown in (*16*)]. Most sediments eroded during plateau uplift were routed through the Recovery Basin and ultimately deposited in the Weddell Sea, where pre–34 Ma sequences reach thicknesses of ~5 km (*31*).

Downloaded from https://www.science.org at University of Southampton on October 15, 2026

Our landscape model predicts ~10 km (total range, 6 to 12 km) of exhumation near the DML escarpment (Fig. 2B and fig. S4). Although high, this estimate is in close agreement with published thermochronologic analyses (Fig. 2C and fig. S6), which indicate maximum erosion of ~13 km near the escarpment (*32*) (or a range of 5 to 9 km, considering only "good fit" models). Model parameters that best reproduce the position and height of the escarpment, plateau, and interior mountains (Fig. 2A, table S1, and figs. S7 and S8) yield thermochronology age predictions (Fig. 2D and fig. S5) that closely match observations (*32*) (Fig. 2E and fig. S6) (see Materials and methods). These results indicate that our landscape model can reliably reproduce the main spatial and temporal patterns of plateau and mountain uplift across the region where the EAIS developed.

### Eocene rejuvenation of the Gamburtsev Mountains

Using predicted two-dimensional (2D) elevations from our model at 2-Myr intervals between 160 and 34 Ma (fig. S4), we reconstructed paleotopography by scaling an existing reference bed topography for the EOT that accounts for post–34 Ma glacial erosion, sedimentation, thermal subsidence, volcanism, and isostasy (*18*). To quantify the potential long-term impact of continental rifting on Antarctic uplift and thus EAIS glaciation, we calculated changes in elevation relative to 34 Ma at each time step (Fig. 2, fig. S4, table S1, and movie S1), generating a time sequence of reconstructed elevation maps (Fig. 3A and movie S2). We further performed a comprehensive uncertainty analysis (table S2) to capture the plausible range of uplift scenarios arising from uncertainties in key model parameters (e.g., Fig. 2A).

Under the most realistic physical conditions for plateau growth (table S1; see Materials and methods), our simulations suggest that mantle-driven waves of uplift and exhumation took ~100 Myr to reach the outer periphery of the Gamburtsev Mountains (movies S1 and S2), implying that the mountains were actively uplifting during the Eocene (Fig. 3B). This is consistent with the development of a mountain fluvial landscape (*21*) later inherited and modified by glaciers to form alpine-style over-deepened valleys (*22*, *23*).

Notably, reconstructed paleotopographies (Fig. 3A) show a sharp increase in Gamburtsev Mountain elevation prior to glaciation. The area fraction of the Gamburtsevs at elevations >2 km is estimated to be <5% at 50 Ma, increasing to >40% at 34 Ma (Fig. 3C). Within our deliberately conservative model based on average elevation changes (see Materials and methods; tables S1 to S3), this Eocene rejuvenation phase produced up to 1 km of total uplift in the Gamburtsevs (Fig. 3A and movie S2). Paxman *et al.* (*21*) estimated that there would be further localized uplift—up to 25% of the peak—resulting from erosional unloading due to valley incision. Mountain uplift in the ~15 Myr preceding the EOT expanded the area above the permanent snow line (*33*), transforming the Gamburtsev Mountains from a largely ice-free, fluvial landscape into a glaciated one.

Eocene uplift in Antarctica was not confined to the Gamburtsevs; thermochronology data indicate sustained, kilometer-scale exhumation across the Transantarctic Mountains (Fig. 1C), initiating between ~55 and 40 Ma (*34*–*36*) and purportedly driven by rifting and lithospheric delamination (*37*, *38*). This uplift coincided with a proliferation of temperate mountain glaciers (*14*) and was coeval with renewed uplift and exhumation in the Antarctic Peninsula and West Antarctica (*34*, *39*) (Fig. 1C; see supplementary text). A component of this activity has been linked to renewed tectonism along the West Antarctic Rift System (WARS), localized along the Ross Embayment bordering the

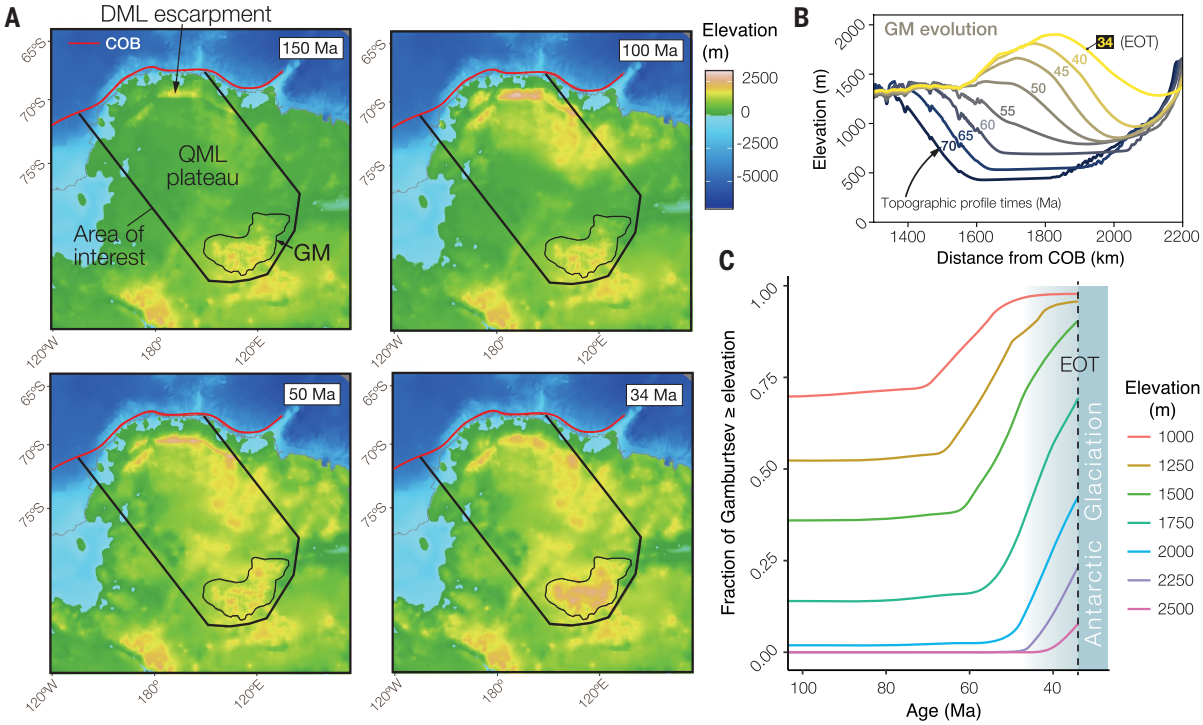


**Fig. 3. Landscape evolution in QML and uplift of the Gamburtsev Mountains.** (**A**) Reconstructed paleotopographies showing the long-term aftermath of continental rifting and breakup, including the formation of the DML escarpment, growth of a continental interior plateau, and rejuvenation of the Gamburtsev Mountains (GM). (**B**) Detail from the landscape evolution model (full profile in fig. S4), showing progressive uplift of the Gamburtsevs from 70 to 34 Ma in the build-up to full EAIS glaciation. (**C**) Area fraction of the Gamburtsevs [outlined in (A)] exceeding given elevations; this shows a marked rise in high elevations (>1750 m) after ~50 Ma. Blue shading indicates Antarctic glaciation and its precursory phase (Fig. 1B). Note that Fastscape parameters are tuned to the 34 Ma median topography, and output is averaged over the model domain *y* axis (parallel to the COB), effectively smoothing out the more extreme peaks (see Materials and methods).

Downloaded from https://www.science.org at University of Southampton on October 15, 2026

Transantarctic Mountains, from ~60 Ma (*37*) (Fig. 1, C and D; see supplementary text). Together with our evidence for persistent uplift and retreat of the DML escarpment (Figs. 2 and 3) and Eocene rejuvenation of the Gamburtsev Mountains, this suggests that uplift occurred synchronously across all three major ice nucleation centers (*4*) during the 20 Myr preceding the EOT.

### East Antarctic uplift seeds glaciation

The critical question, then, is whether the inferred location and magnitude of bedrock uplift (Figs. 2 and 3) were sufficient to influence ice sheet nucleation and expansion. To address this, we utilized the Parallel Ice Sheet Model (PISM; https://www.pism.io/), an open-source modeling framework for ice sheets and glaciers that incorporates ice flow and marine ice behavior (*40*). Our model incorporates geothermal heat flux based on up-to-date seismic tomography and lithospheric structure (*41*) (fig. S9) and applies temperature and precipitation boundary conditions for the region informed by HadCM3L climate simulations (*42*) (see Materials and methods; fig. S10 and tables S4 and S5). Using 12 paleotopography reconstructions (e.g., Fig. 3A), we generated quasi–steady-state ice thickness after a 20,000-year spin-up from an ice-free landscape (fig. S11). Although the climate (e.g., aridity) of the East Antarctic interior prior to the EOT is uncertain, we assumed coastal precipitation rates and a temperature-precipitation scaling that are consistent with empirical findings (see Materials and methods). Our models suggest that mountain ice caps can be sustained in the Gamburtsev Mountains with relatively low annual precipitation rates (~250 m/Myr).

Our simulations indicate that dynamic uplift seeded ice cap formation in the Eocene Gamburtsev Mountains (Fig. 4A). This result aligns with suggestions that dynamic topography can influence the cryosphere by controlling ice sheet equilibrium geometry (*43*). In this study, however, we explicitly examined the spatial and temporal evolution of topography in response to multimillion-year mantle wave-driven uplift and exhumation across the East Antarctic landscape (Figs. 2A and 3), which specifically considers a realistic evolution of solid Earth boundary conditions to EAIS growth (Fig. 4A). Holding climate constant, we identified a topographic threshold for ice cap nucleation at ~50 to 45 Ma (Fig. 4B and fig. S12), when the fraction of highlands rises sharply and more than half the land exceeds 1500 m elevation (Fig. 3C). To assess the climate dependence of the timing of this threshold, we conducted sensitivity tests that explore the impact of varying initial climate conditions, from warm to cold end members informed by estimated uncertainties in global mean surface temperature (GMST) during the Eocene (*44*) (fig. S13; see Materials and methods). Although accelerated ice accumulation starts earlier (~58 Ma) in cold climate scenarios and later (~46 Ma) in warm ones, crucially, these variations do not change the presence of a threshold for ice sheet assembly when Antarctica's cryosphere substantively emerged (Fig. 1B) (*13*, *14*, *27*).

### Interplay of uplift and global cooling led to EAIS formation

Climate models indicate extreme seasonality in the late Eocene, featuring short, intense summers and long, cold winters (*17*). These conditions caused nascent ice caps to wax and wane, perhaps for 10 to 15 Myr before the EOT (Fig. 1B). Our models indicate that major ice sheet expansion occurred when terrain uplift (Fig. 4) and global cooling, driven by declining atmospheric $CO_2$ (*4*, *5*) (Fig. 1A), together reached a critical threshold (figs. S12 and S13). This threshold likely marks the onset of self-stabilizing hysteresis in early ice sheets that enabled sustained glaciation despite intervening insolation-driven warming cycles (*45*).

To quantify how uplift and global cooling acted jointly to stabilize the EAIS, we used a conceptual energy balance model (EBM) that integrates observational data with fundamental climate physics. Our EBM features explicit cloud representation for short- and long-wave radiation, latitudinal albedo feedbacks constrained by modern observations (*46*), and climate state–dependent poleward heat transport,

Downloaded from https://www.science.org at University of Southampton on October 15, 2026

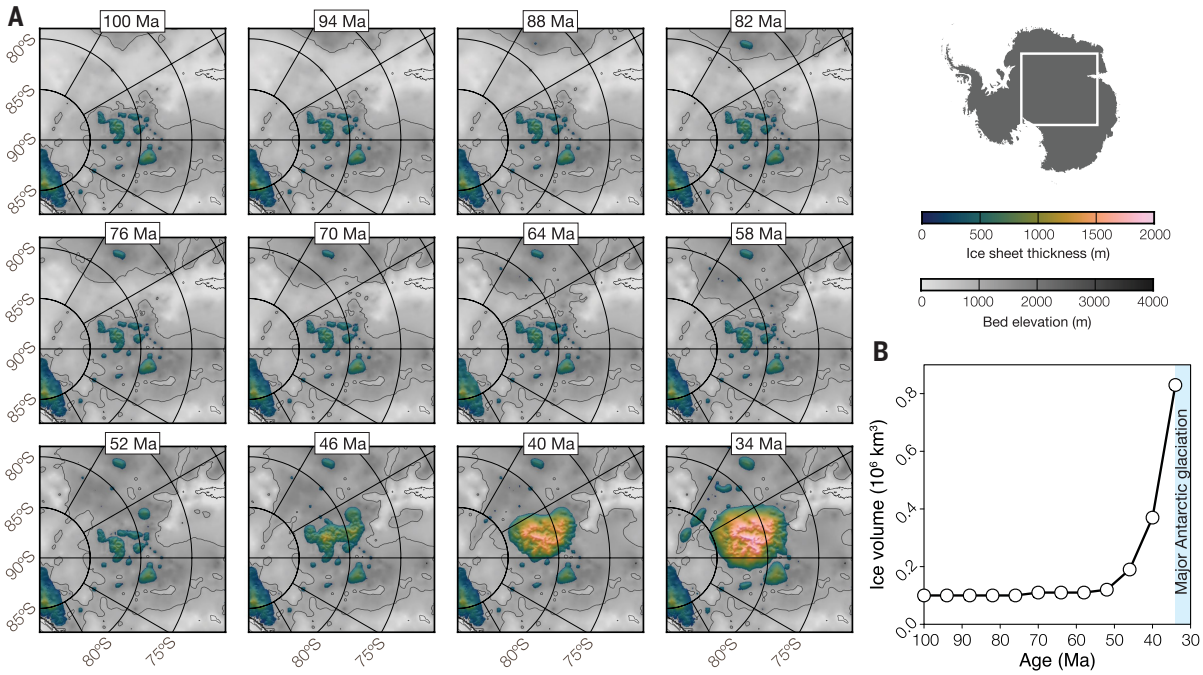


**Fig. 4. East Antarctic uplift drives spatial expansion of Antarctic ice caps.** (**A**) Results from our PISM experiments show the spatial extent of ice of a given thickness in response to the reference topographic model (Figs. 2 and 3), at 6 Myr intervals from 100 to 34 Ma, for fixed climate conditions. The sequence captures the development of a major ice cap over the Gamburtsev Mountains, a process that is highly sensitive to the underlying topography. (**B**) Modeled ice volume through time for the same reference case, revealing a threshold crossed at ~50 Ma (for $m_{seq}$, see fig. S12). The sensitivity of the timing of this threshold to warm versus cold climates is shown in fig. S13.

in which diffusivity varies with Clausius-Clapeyron–controlled humidity and yields polar amplification consistent with observations (*47*). In this work, we updated this model (see Materials and methods) to (i) account for the relationship between Antarctic Ice Sheet thickness and surface temperature, such that maximum elevation is capped to present-day levels to implicitly account for isostatic loading by ice sheets; (ii) introduce a lapse rate to adjust surface temperatures by elevation at present-day resolution before diffusing heat meridionally; and (iii) include an ice trapping function to reflect reduced insolation at polar latitudes (fig. S14), which promotes ice accumulation between alpine mountain peaks that lie in near-permanent darkness.

Paleodata show a robust near-linear relationship between the latitudinal temperature gradient (defined from the tropics to the Southern Ocean) and global temperature over the past 90 Myr (−0.66° ± 0.21°C per °C) (*8*). Our EBM reproduces this behavior within uncertainty (slope = −0.84; coefficient of determination $R^2$ = 0.97; fig. S15), capturing Southern Hemisphere polar amplification more faithfully than most of the more complex Earth system models evaluated in (*8*), making our EBM highly suitable for simulating Antarctic cooling.

Using this EBM, we calculated GMST and corresponding minimum elevation for ice sheet growth in 1° latitudinal bands from 75°S to 85°S (e.g., fig. S14) given values of radiative forcing (RF) from 0 to 20 $Wm^{-2}$. By combining these outputs with reconstructed topographies (Fig. 3), we estimated the theoretical maximum GMST needed to sustain ice at each elevation and time slice (Fig. 5A) and compared these with published paleotemperature records by Judd *et al.* (*44*) and Scotese *et al.* (*48*) (fig. S16) to identify areas capable of sustaining ice cover. This model framework allows us to determine how a key part of East Antarctica's cryosphere, spanning the Gamburtsev and Transantarctic Mountain regions and the QML plateau, responded to the combined effect of uplift and evolving GMST since 100 Ma. The relatively warm GMST record of Judd *et al.* (*44*) indicates (theoretically) a scarcity of ice until ~36 Ma, followed by only patchy cover in the higher parts of the Gamburtsevs (Fig. 5A). By contrast, the cooler GMST of Scotese *et al.* (*48*) permits ice sheet expansion across the rising Gamburtsevs and adjacent plateau from ~48 Ma, with near-complete coverage across the study area by ~34 Ma (Fig. 5A). In practice, a scenario midway between the two GMST records (*44*, *48*) aligns well with both our EBM outputs (Fig. 5) and the independent ice sheet parameterization (Fig. 1B). The EBM results further show that topographic uplift permits ice accumulation under GMST up to 1°C warmer than normally expected (fig. S17).

We next used the EBM outputs to assess how our reconstructed topographic uplift scenarios (Fig. 3) between 100 and 34 Ma affect the minimum elevation for ice stability (Fig. 5B). Assuming a representative GMST of 19°C for the EOT (*48*), East Antarctic uplift lowered the threshold elevation for ice by 500 m at 75°S and 700 m at 85°S (Fig. 5B), which is a substantial shift. Uplift across the QML plateau and Gamburtsev Mountains both lowered the elevation at which ice could form and expanded the area above the ice stability threshold, with the greatest

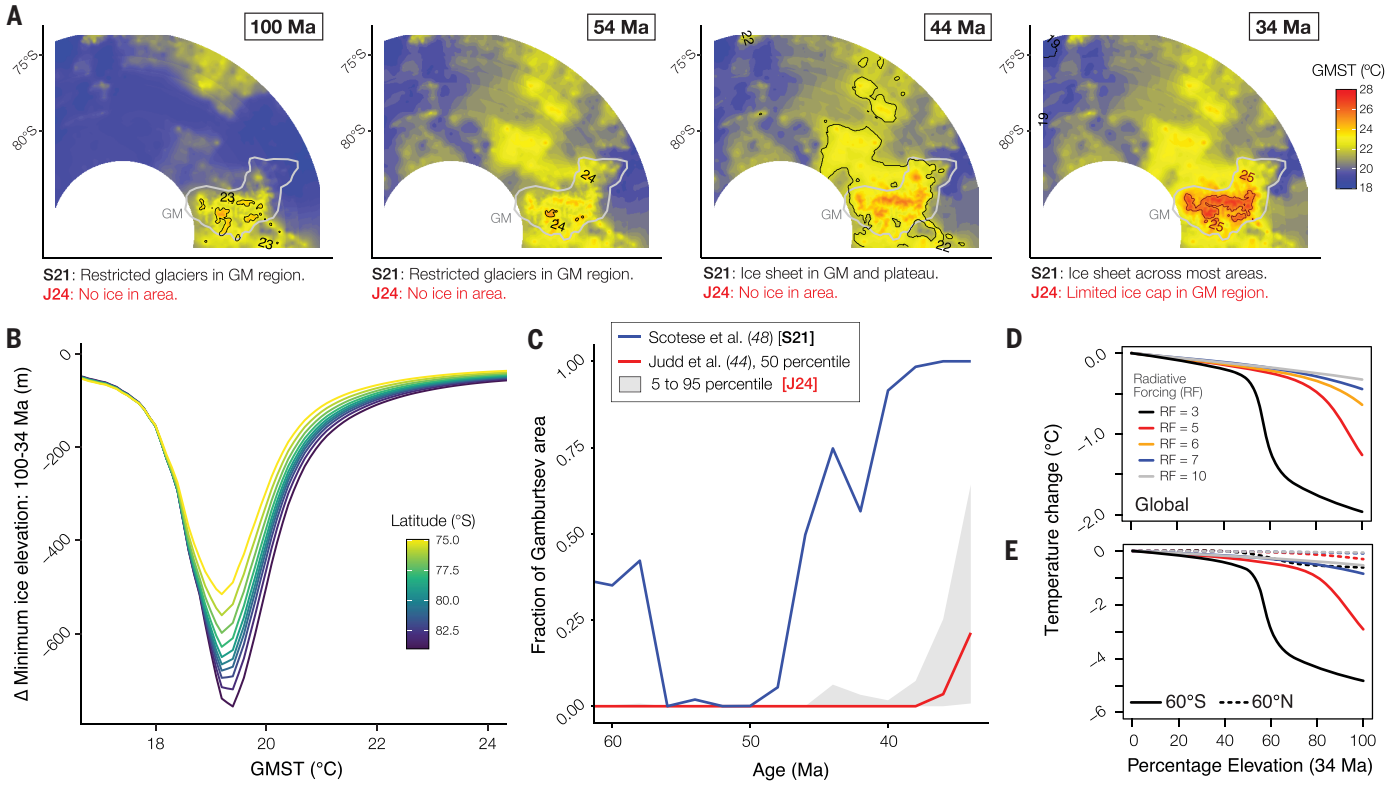


**Fig. 5. Interplay of regional uplift and global cooling in EAIS assembly.** (**A**) Maps showing the theoretical maximum temperature that would sustain ice at that elevation for four time slices: 100, 54, 44, and 34 Ma. Contours delineate regions where ice formation is viable at prevailing temperatures, based on two GMST records: the 50th percentile from (*44*) (J24) and the record from (*48*) (S21). These maps illustrate the likely extent or, indeed, absence of ice. (**B**) Change in the minimum elevation required for ice stability between 100 and 34 Ma, shown by 1° latitude bands (colors). (**C**) Fraction of the rising Gamburtsev Mountains (Fig. 3) where ice could theoretically accumulate over time based on GMST reconstructions from J24 (*44*) and S21 (*48*). (**D**) Modeled changes in GMST as a function of changing topographic elevation (expressed as a percentage of the 34-Ma elevation) under different RF values. The maximum global cooling shown (2°C) represents an upper-end scenario, whereas a reduction of 1°C is considered more likely. (**E**) Same model as in (D), showing the change in temperature at 60°N and 60°S as a function of changing topography, based on a representative location at 85.5°S; this highlights an asymmetric response between hemispheres, with the Southern Hemisphere showing a stronger temperature response to uplift and glaciation than the Northern Hemisphere.

Downloaded from https://www.science.org at University of Southampton on October 15, 2026

impact occurring when GMST fell below ~21°C (Fig. 5B). Specifically, we found that the ice-sustaining fraction of the Gamburtsev Mountains increased from 0 to 20% (by area) between 60 and 34 Ma using the GMST reconstruction of Judd *et al.* (*44*) and from 35 to 100% using that of Scotese *et al.* (*48*) (Fig. 5C). Under both scenarios, the studied region's capacity to host ice rose sharply from ~40 Ma (Fig. 5C), consistent with probabilistic ice sheet coverage estimates (Fig. 1B).

In addition to demonstrating how geodynamically forced landscape evolution can precondition East Antarctica for glaciation, this coupled landscape–ice sheet–climate model framework can reconcile the polar climate asymmetry of the Oligocene, a highly enigmatic feature of existing models (*7*). This asymmetry is marked by a stark contrast in temperature and ice cover between the Northern and Southern Hemispheres, with relatively warm high-latitude conditions persisting despite modest global cooling and extensive Antarctic glaciation (Fig. 1B). Our EBM indicates a ~1.0°C reduction in GMST resulting primarily from the final 20 to 30% of uplift required to reach EOT topography (Fig. 5D), reflecting albedo feedback as the uplift glaciates Antarctica. The uplift can thus explain the modest global mean cooling observed across the EOT (*8*), with relatively warm Southern Ocean conditions (*7*) that appear inconsistent with continental glaciation. The model shows only a minor (<1°C) temperature response in the (lower-elevation) Northern Hemisphere (Fig. 5E), as expected, where ice sheet formation did not begin until ~10 Ma (*6*, *49*), pointing to a local stimulus for EAIS formation.

## Discussion

We propose that the sequence of geodynamic, geomorphic, climatic, and glacial changes (Figs. 2 to 5), ultimately set in motion by Gondwana's breakup (fig. S2), led directly to EAIS inception and growth more than 120 Myr later. These changes enabled the Gamburtsev Mountains to accumulate and shed ice onto a broad, elevated plateau (Fig. 3), bounded to the north by the DML escarpment (Fig. 1C), a major drainage divide and itself also a (long-term) nucleation site for ice caps (*4*, *13*). Our EBM results indicate that this plateau was sufficiently elevated to sustain an ice sheet by ~45 to 40 Ma (Fig. 5A). By contrast, the narrow extent and flanking lowlands of the Transantarctic Mountains (Fig. 1C) limited their capacity to support a large ice cap. The uplifting Gamburtsev Mountains and QML plateau (Fig. 3) thus served as a vast focal point for rapid ice sheet expansion across East Antarctica after ~40 Ma, as elevations rose and temperatures fell (Fig. 5A). This tight coupling of uplift and cooling helps explain an abrupt transition from fluvial to glacial erosion (*20*, *21*) and how a cold-based, nonerosive ice sheet could establish before dendritic fluvial valley networks were fully reshaped by mountain glaciers (*22*, *23*).

Notably, we found that Antarctic uplift did not appreciably affect high-latitude temperatures away from the ice sheets (e.g., over oceans; Fig. 5, D and E), consistent with proxy records (*7*). Thus, an Eocene uplift scenario for Antarctica can explain not only the timing of EAIS glaciation but also the enigmatic Oligocene climatic warmth extending to the high-latitude Southern Ocean (*7*). EAIS formation is typically attributed to $CO_2$-driven cooling (*4*, *5*) linked to enhanced silicate weathering primarily during Himalayan mountain uplift (*9*). However, recent observations indicate that $CO_2$ drawdown peaks at moderate erosion rates, well below those typical of active mountain belts (*50*). Additionally, oxidation of organic carbon can offset weathering-driven $CO_2$ consumption (*51*), suggesting that the net climatic impact of rapid uplift in collisional orogens may be more complex than previously assumed. Rather, the climatic conditions conducive to ice sheet formation likely arose from a confluence of tectonic and paleogeographic factors (*10*), which extend beyond rock weathering alone.

It must be noted that the opening of Southern Ocean gateways, such as the Tasmanian and Drake Passage or Scotia Sea gateways, has also been proposed [though this is debated (*52*)] as a primary driver of EOT cooling through initiation of the Antarctic Circumpolar Current and subsequent thermal isolation of the continent. Trans-Antarctic seaways may too have existed in early Oligocene West Antarctica, but if present, they were likely shallow and restricted by bedrock ridges (*13*). Sedimentologic evidence indicates that deep-water exchange through Southern Ocean gateways remained limited at the EOT (*31*). Moreover, $TEX_{86}$-based sea surface temperature records suggest that full deep opening did not occur until ~26 Ma (*53*). Only thereafter were stronger deep currents and sustained circumpolar flow [and thus substantial cooling (*54*)] established, too late to have been a first-order driver of EOT cooling and EAIS glaciation.

Instead, a critical but overlooked factor is the long-term continental breakup–related uplift identified in this work (Figs. 2 and 3). This process is demonstrably sufficient to push landscapes beyond the threshold for ice sheet nucleation (Figs. 4 and 5). The polar position of Antarctica during this Eocene uplift, which likely affected large parts of the continent (Fig. 1C), made it unusually sensitive, amplifying local cooling and enabling widespread glaciation. This system of landscape–ice sheet–climate coevolution is a powerful driver of glaciation that could have influenced earlier glaciations, including the Late Paleozoic Ice Age (~360 to 255 Ma), when most landmasses occupied the Southern Hemisphere (*10*). Because the Eocene uplift reported in this work occurred locally in Antarctica (Figs. 1C and 3), it could initiate Southern Hemisphere glaciation (Figs. 4 and 5), whereas the Northern Hemisphere remained substantively ice free. This mechanism can thereby help explain the pronounced ~20 Myr delay in Northern Hemisphere glaciation relative to that of Antarctica.

## Materials and methods

### Landscape evolution models

Building on (*16*), we apply Fastscape (*55*, *56*) to model uplift and erosion resulting from the propagation of an organized wave of surface uplift driven by dynamic mantle processes originating along the continent-ocean boundary (COB; for location, see Fig. 3) at approximately 160 Ma (see Supplementary Text). Fastscape is a well-documented, open-source toolkit for landscape evolution modeling, solving the stream power law and flexure equations in two dimensions (i.e, x and y directions) to compute vertical surface displacement and erosion (*16*, *28*).

A local topographic high in the Gamburtsev Mountain region likely developed through flexural uplift of the Lambert Rift margin in the Mesozoic (*29*), exerting a control on erosion and sedimentation patterns. However, it must be noted that other models for the mountains' origin invoke far older tectonic events, from Pan-African orogenesis (*57*) to Pangaea assembly (*58*), though these are difficult to reconcile with the present-day geomorphology (*20*–*23*). Even within a Permo-Triassic rifting framework (*29*), flexural uplift alone cannot explain the reniform (i.e., not rift-parallel) geometry of the mountains, the persistence of the alpine-like relief, the associated fluvial weathering patterns, nor the connection of these mountains to the adjacent QML plateau—features that we argue are fundamentally connected (c.f. (*16*)) (figs. S1 and S2).

In our landscape evolution model, the initial topography is defined as a low-relief continental region (h0; table S1), informed by landscape evolution models for southern Africa (*16*) and average elevations of Archaean and Proterozoic cratons in Australia—then contiguous with Antarctica—of approximately 280 m (*59*). Because our landscape model spans back to 160 Ma and includes the Lambert Graben side of the Gamburtsevs (fig. S1), the initial profile incorporates a step up in the Gamburtsev region ($h0_g$) of an additional 1,100 m (table S2), reflecting elevated paleotopography linked to rifting along the Lambert Graben between ~250 and ~100 Ma (*29*). This topographic step lies within the upper range of average elevations for Precambrian cratons globally (*59*) and would invariably have influenced erosion and sedimentation patterns during the 160–34 Ma interval considered in our model.

Narrow, focused rift systems, such as that which initiated between Africa and Antarctica around 177 Ma (fig. S2), are commonly associated

Downloaded from https://www.science.org at University of Southampton on October 15, 2026

with prominent marginal escarpments and, at depth, physically steep gradients of the lithosphere-asthenosphere boundary. These steep gradients promote edge-driven convection during phases of accelerated rifting and continental breakup, initiating Rayleigh-Taylor-type instabilities that can propagate slowly inboard along the continental keel, disturbing the sub-cratonic thermal boundary layer. Given the presence of a pronounced crustal and lithospheric step beneath the Africa-Antarctic rift (*60*), the presence of a steep marginal escarpment, and the tectonic context of cratonic breakup (supplementary text), we infer that this process operated similarly in what was then the contiguous lithospheric domain of southern Africa (*16*) (noting that the landscape features and associations are very similar). To capture this dynamic, we impose a propagating front of lithospheric destabilization and associated isostatic uplift using a Gaussian function, with a velocity of 15 km $Myr^{-1}$ and a half-Gaussian width of 200 km, informed by prior geodynamic modeling work (*15*, *16*, *61*).

The amplitude is set to achieve the target plateau height ($h_{plateau}$) after isostatic adjustment and given initial topography (h0). Subsequent erosion over the duration of the simulation reduces this plateau height, with the target of reaching the known elevation at 34 Ma [i.e., reconstructed topography from Paxman *et al.* (*18*)]. The full set of inputs for the best fit model are given in table S1, with parameter ranges to accommodate uncertainty given in table S2. Inputs were informed by both thermomechanical simulations (*15*, *16*) and published crustal parameters for Antarctica [e.g., (*62*); fig. S3]. Final parameter tuning was applied to determine a 'best fit' model (given known parameter constraints/ranges), using the Python library Mango (*63*) (https://github.com/ARM-software/mango). A misfit function was defined to penalize differences between the simulated topography and median 34 Ma reconstructed topography of Paxman *et al.* (*18*) over the area of interest (Figs. 2A and 3) at key locations on the escarpment, main QML plateau and the Gamburtsev Mountains (Fig. 1D and fig. S1). This yields a simulated topography that replicates the key features of the best known pre-glacial landscape (Fig. 2 and Movie S1).

Model inputs for the effective elastic thickness ($T_e$) of the lithosphere use a best-fit value of 35 km, with uncertainty analysis spanning 25–55 km (table S2). These values are informed by estimates from (*62*) across the region of interest (fig. S3), and further refined through parameter tuning. We note, however, that $T_e$ is often overestimated in such models (*64*).

Sensitivity tests reveal that varying the width of the imposed Gaussian wave width within reasonable bounds (±50 km) made no significant difference to the simulation outcomes; hence, this parameter is held constant. At 160 Ma, the elevation of the Gamburtsev region in the model (fig. S1) is assumed to be ~1,400 m ($h0 + h0_g$), based on crustal estimates from gravity models of this region (*29*), and constrained by the model fit to reconstructed topography at 34 Ma.

To predict thermochronology ages, we use the same algorithms used in the Pecube software (*65*), following the method of (*16*). We adopt a most-likely geothermal gradient of 25°C $km^{-1}$, consistent with estimates for Eocene Antarctica (*66*, *67*). A broader gradient range of 20–30°C $km^{-1}$ is also considered to capture the likely range of conditions (see fig. S5).

### Resolution and boundary conditions

To match the scale of Antarctic physiography, we limit the horizontal extent of the landscape model analysis to 2,500 km, while extending the model domain to 3,500 km to minimize potential boundary effects (that is, through the right-hand boundary). The domain is a narrow strip discretized at 1 km resolution, with an extent of 3,500 km in the x-direction and 40 km in the y-direction. Simulations are run from 160 to 34 Ma with a time step of 0.1 Myr, outputting elevation and cumulative erosion fields every 2 Myr. Thermochronological modeling for prediction of apatite (U–Th)/He (AHe) and apatite fission-track (AFT) ages spans the period from 160 to 15 Ma, enabling estimates of crustal cooling ages during the interval when Antarctic glaciers—particularly those near the coast (i.e., along the DML escarpment, currently the only region where model predictions can be robustly tested)—advanced and retreated during prolonged Oligocene and Miocene interglacials (*26*), prior to AIS stabilization later in the Miocene (Fig. 1B) (*6*, *24*).

In all model runs, the boundary conditions are as follows: left - open; right - fixed; back - open; front - fixed. This ensures material eroded from the 'left' flank of the escarpment can flow offshore rather than accumulate at the boundary and can also 'exit' the system via the back boundary, between the escarpment high and elevated Gamburtsev region. Without an open back (or front) boundary, the bounding features of the Gamburtsev Mountains and escarpment prevent any loss of material from the plateau region, resulting in a sector with unrealistic erosion and age estimates.

### Parameter tuning

'Best-fit' model parameters were determined using Mango (*63*), which minimizes a misfit function, $\mu$ (*16*), quantifying deviations between the simulated topography and the median topography of the 34 Ma reconstruction (table S3) for the main landscape features shown in fig. S1. Note that the x-coordinates are expressed relative to the present-day continent-ocean boundary (COB; Fig. 3), and are offset by 100 km in the model reference frame. Because the distance between the COB and the escarpment varies along strike, we instead calculate elevation within a 20 km-wide zone encompassing the escarpment peak (Fig. 2A, inset). The target elevation of 1,850 ± 100 m lies between the mean (1,840 m) and median (1,886 m) elevations within this zone.

We calculate misfit values for multiple model runs (figs. S7 and S8) in which two parameters are varied simultaneously—that is, $T_e$ and the erodibility coefficient $K_f$ (fig. S7A), or uplift wave velocity ($v$) and $K_f$ (fig. S7B). A smaller misfit indicates a closer match to the target 34 Ma topography, based on six key topographic features (fig. S1 and table S3): the position and elevation of the escarpment; average elevation across the plateau; the ramp leading up to the Gamburtsevs [simulating pre-existing topography associated with the Lambert Graben (*29*)]; the Gamburtsev peak; and the lower-elevation region beyond the peak (fig. S8 and table S3). Note that determining a good fit also requires manual inspection of the output, as there can be unrealistic topographic features outside the scope of the misfit function. All other parameters are fixed at their 'best fit' values (table S1). Models are run from 160 to 34 Ma, with the final topography (at 34 Ma) used to compute misfit. In the misfit plots related $T_e$, $K_f$ and $v$ (fig. S7), the parameter values for the 'best fit' model run (see table S1) are shown as red dots, which yield low misfit scores.

### Topographic reconstructions from 160 to 34 Ma

Best-fit parameters were used to generate topographic reconstructions simulating potential landscape change from 160 to 34 Ma, at 2 Myr intervals (Fig. 3 and movie S2). Starting from a simple, stepped initial topography—comprising a low continental plateau beginning at the COB and a secondary elevation step in the Gamburtsev region (tables S1 and S2)—we run Fastscape and compute the mean elevation across the y-dimension to produce 2D elevation profiles at each time-step, $f(x,t)$, where $x$ is distance relative to the COB and $t$ is time.

We then compute the fractional and relative differences in modeled elevation at $t$ and at 34 Ma using the expressions $\frac{f(x,t)}{f(x,t=34\,Ma)}$ and $f(x,t) - f(x,t=34\,Ma)$.

The 34 Ma topography of (*18*) is used as the baseline, as it represents the oldest reliably reconstructed surface (5 km grid, EPSG:3031—WGS 84 Antarctic Polar Stereographic projection). For each raster cell we compute the distance $d$ to the nearest section of the COB (as defined at 160 Ma; Fig. 3), and then derive a modified elevation $e'(d,t)$ at each time step $t$, where $e(d_{lat,lon}, 34Ma)$ denotes the baseline 34 Ma elevation [from (*18*)] for the raster cell at coordinates (*lat,lon*) and distance to COB $d$.

Downloaded from https://www.science.org at University of Southampton on October 15, 2026

(i) If the baseline map elevation $e(d_{lat,lon}, 34Ma)$ is less than or equal to the Fastscape model elevation $f(d, 34Ma)$ then the modified cell elevation is calculated as:

$$e'(d_{lat,lon}, t) = e(d_{lat,lon}, 34Ma)\ f(d, t)/f(d, 34Ma) \quad (1)$$

(ii) If the map elevation $e(d_{lat,lon}, 34Ma)$ is greater than the model elevation $f(d, 34Ma)$ then the modified cell elevation is calculated as:

$$e'(d_{lat,lon}, t) = e(d_{lat,lon}, 34\text{Ma}) + f(d,t) - f(d, 34\text{Ma}) \quad (2)$$

(iii) If $e(d_{lat,lon}, 34Ma) \leq 0$ m the cell elevation is unchanged.

Adding rather than scaling the highest elevations prevents the generation of unrealistically extreme highs in the modified topography. This is a conservative approach as our best fit model, used to determine the scaling cutoff, is based on median elevations from the 34 Ma reference map (*18*). Peak elevations greatly exceed these values (see Fig. 2A), with such uplift likely reflecting erosional unloading in response to valley incision (*21*). We do not attempt to reconstruct points at or below sea level, as these lie outside the model domain and are not relevant within the area of interest.

### Model limitations

There are limitations to the above approach, namely that it cannot fully model the development or evolution of erosional channels, changes to coastlines or inland water bodies, and any subsequent impact on isostatic rebound. Nevertheless, it provides a physically plausible and likely conservative estimate of topographic changes over time for the QML plateau and Gamburtsev Mountains.

Further, Fastscape does not incorporate glacial erosion, resolving only stream power incision and diffusion (*16*, *28*). Nevertheless, because we focus on plateau growth in the pre-glacial interval—particularly the warm Eocene, which was dominated by fluvial systems (*68*) including in the Gamburtsevs (*21*)—this is considered a reasonable approach. Although mountain glaciers likely developed in the Transantarctic Mountains (which is not a focus of our landscape modeling) by ~40 Ma (Fig. 1C), geomorphic evidence from the Gamburtsev Mountains indicates that fluvial landscapes persisted until rapid ice sheet takeover in the Late Eocene, as suggested by the abundance of alpine-type valleys, and the relative scarcity of glacially exploited (i.e., U-shaped) valley systems (*21*–*23*). Similarly, landscapes of Dronning Maud Land record substantial (~1 km) fluvial incision that was later overprinted (but not obliterated) by mountain glaciation, as indicated by arêtes, cirques, valley overdeepenings, and closely spaced hanging valleys (*69*). Thus, glacial erosion in the Gamburtsev and Dronning Maud Land Mountains was transient and unlikely to have influenced the broad-scale landscape evolution captured by our models.

Directly testing our landscape model is difficult due to thick ice sheet cover, although the predictions are consistent with the observed subglacial geomorphology (*20*–*23*). Our model can, however, estimate thermochronologic ages for the apatite (U–Th)/He (AHe) and apatite fission-track (AFT) systems (*16*), which can be tested against observations in restricted regions of exposed bedrock, specifically along the DML escarpment (*32*, *70*) (Figs. 1D and 3 and fig. S6). Comparing modeled and observed ages along this escarpment (*32*), particularly the youngest resetting ages, shows good agreement for a crustal geothermal gradient of 25°C $km^{-1}$ (Fig. 3). This value is slightly higher than the present-day Antarctic average (~20°C $km^{-1}$) (*41*) (i.e., featuring a continental ice sheet), and is consistent with gradients inferred for Eocene East Antarctica (*66*, *67*) and with median gradients reported for South Africa (*16*). Notably, AHe and AFT age resetting occurred predominantly before 40 Ma (Fig. 2E and fig. S6), which suggests that escarpment formation dominated over glacial erosion. We infer limited erosional reworking by glaciers and thus rapid ice sheet nucleation, consistent with earlier studies (*4*, *22*, *71*).

Detrital thermochronology, such as that from Prydz Bay (*30*), offers potential constraints, though the provenance of these grains is uncertain and unlikely to provide a spatially representative sample of the Gamburtsev Mountains. At present, rigorous testing of our model in the distal parts of the QML plateau and Gamburtsev Mountains is not feasible, but future sub-ice drilling of bedrock could provide direct sedimentologic and thermochronologic evidence to further test our model.

### Ice sheet models

We conducted a series of simple ice growth experiments to assess how landscape evolution over time, and specifically the resulting variations in bed topography, may have influenced ice sheet formation and stability. Previous studies have explored the sensitivity of the Antarctic Ice Sheet to evolving bed topography during past warmer climates and potentially into the future [e.g., (*27*, *72*, *73*)]. In contrast, our approach reverses the problem, examining how pre-glacial topographic changes may have influenced the timing and magnitude of ice sheet nucleation.

We used the PISM (https://www.pism.io/), an open-source numerical framework for ice sheets and glaciers which accounts for ice flow and marine ice dynamics (*40*). We used PISM in its 'hybrid' mode, which simulates internal deformation and basal sliding by applying the shallow-ice and shallow-shelf approximations, respectively. Unless otherwise stated, we used the PISM default values for the model parameters relating to ice rheology and basal sliding (table S4). Our implementation largely follows that of previous studies [e.g., (*74*)], with several updates. Our specific focus is on the changes affecting the highland region of central East Antarctica, specifically within the Gamburtsev Mountains (Fig. 1C), where East Antarctic Ice Sheet nucleation is believed to have initially occurred (*20*, *22*).

The boundary conditions for our experiments includes geothermal heat flux (fig. S9B), which was derived from the most up-to-date seismic tomography and lithospheric structure (*41*) (table S5). Additionally, we used a series of 12 bed topography reconstructions (that is, every 6 Myr) spanning from 100 Ma to 34 Ma (movie S2), with the "final" topography at 34 Ma based directly on the reconstructions of Paxman *et al.* (*18*). This Eocene-Oligocene reconstruction accounts for processes including glacial erosion, sedimentation, thermal subsidence, volcanism, and isostasy. All these reconstructions represent ice-free landscapes that are in isostatic equilibrium.

Experiments are forced with a fixed climate starting from an ice-free landscape (fig. S9A and tables S4 and S5) with a horizontal grid resolution of 10 km. Each model was run for 20 thousand years (kyr), by which point quasi-equilibrium had demonstrably been achieved in each case (fig. S11). Isostatic adjustment and ice elevation-mass balance feedbacks are included in the model (*40*).

The core ice sheet model experiment was forced by a climate defined by a mean annual air temperature (MAAT) at sea level at 65°S (i.e., the approximate latitude of the East Antarctic coast) of 10°C (table S5), a representative value for the late Eocene derived from paleoclimate records and models (*42*, *44*, *75*, *76*). A latitudinal temperature gradient of -0.3°C/°S and an adiabatic lapse rate of -6.5°/km were applied, along with a seasonal cycle of ±10 °C (*44*, *75*, *77*). MAAT forcing for the ice sheet model experiments (illustrated for the 34 Ma topography) is shown in fig. S10A and the annual precipitation for the ice sheet model experiments (again for the 34 Ma topography) is shown in fig. S10B.

Following empirical findings (*78*), we set a baseline annual precipitation of 250 mm $yr^{-1}$ at the lowest temperatures, scaled by 5.5% per °C. This yields coastal precipitation of ~1,200 mm $yr^{-1}$, comparable to modern Patagonian analogs (*79*, *80*) and modeled Eocene climatologies (*81*). These coastal precipitation rates are also consistent with the presence of *Nothofagus* (southern beech) in Eocene-Oligocene Antarctic margin sediments, taxa which today thrive in cool-temperate Patagonia (~5 to 10°C MAAT) under annual precipitation exceeding 1,500 mm $yr^{-1}$ (*79*), as noted by (*13*).

Downloaded from https://www.science.org at University of Southampton on October 15, 2026

While some Earth System Model simulations suggest that the Gamburtsev Mountains were too arid to support early ice sheet nucleation (*13*), this view is difficult to reconcile with geomorphic constraints. Subglacial observations reveal a once-highly-active fluvial landscape—similar to that of Dronning Maud Land (*69*)—that was subsequently overprinted, but not erased, by alpine glaciation (*22*). This geomorphic record implies sufficient paleoprecipitation prior to the Eocene-Oligocene boundary to sustain both fluvial systems and subsequent valley glaciers. Indeed, our modeling suggests that mountain ice caps can be sustained with relatively low annual precipitation rates (~250–300 mm $yr^{-1}$; Fig. 4 and fig. S10). It is feasible that adjacent low-lying parts of East Antarctica were occupied by lakes or inland seas prior to widespread glaciation, providing a local moisture source. Indeed, geomorphic analysis suggests that the base level of some Gamburtsev fluvial catchments was controlled by enclosed interior (i.e., lake-filled) basins associated with extensional faulting (*82*). Moreover, elevations in the Gamburtsevs (Fig. 3, B and C) may have been sufficiently high to generate substantial orographic precipitation. Crucially, the Gamburtsevs' landscape is characterized by landforms eroded by mountain-scale ice caps radiating from central highlands (*22*), a signature that is inconsistent with the Gamburtsevs being situated on the periphery of a large ice sheet, or erosion via later ice sheet overriding. These features necessitate the existence of early, restricted ice centers on the Gamburtsevs and DML prior to continental-scale ice sheet expansion.

For the older (i.e., Cretaceous) topographies, it must be noted that the imposed climate in our models is substantially colder than would have prevailed at the time. This approach is intentional: by holding climate constant, we isolate the influence of evolving topography on ice-sheet growth. Still, we emphasize that these simulations, particularly those for the Cretaceous, are designed to test topographic sensitivity rather than to reconstruct the absolute presence (or indeed absence) of ice during those periods.

For each time slice, and thus each paleotopographic reconstruction, we ran identical ice sheet-climate simulations to test the sensitivity of our results to the uncertain background climate state. We explored this uncertainty by considering climates within ±2°C of our core experiment, representing 'cold' and 'warm' end-members. This range captures the uncertainty in starting temperatures, based on recent global mean surface temperature (GMST) records, which suggest an uncertainty of about 1.5°C to 2.0°C at the Eocene-Oligocene boundary (*44*) (fig. S16). The equilibrium ice volume of the modeled ice sheet as a function of topography is shown in figs. S13A and S13B for the cold and warm end-members, respectively. Both scenarios point to the crossing of a topographic threshold for ice-cap growth, albeit at different times: ~58 Ma under the colder climate scenario and ~46 Ma under the warmer one. Crucially, neither scenario changes our main conclusion that a threshold was reached during the broader time window in which the cryosphere likely emerged across Antarctica's highlands (Fig. 1B).

### Energy balance models

The Energy Balance Model (EBM) of Goodwin and Williams (*47*) is used, solving for outgoing long-wave radiation, outgoing shortwave radiation, horizontal poleward heat flux and temperature with latitude. Here the EBM is reconfigured to have 1° resolution in latitude, with a prescribed fraction of land and ocean at each latitude. The equations describing outgoing long-wave radiation with latitude and outgoing shortwave radiation with latitude are updated to the observation-constrained equations within (*46*). Since these updated equations have different albedo and planetary emissivity coefficients over land and over ocean (*46*), here the albedo and planetary emissivity for each latitudinal band are calculated for land and ocean separately and then linearly combined according to the faction of land and ocean at that latitude.

For latitudes from -90° to -75° the height of the Antarctic ice sheet is solved for in the following way. The probability distribution of elevation above sea level for underlying land is calculated for each 5° band (−90° to −85°, −85° to −80° and −80° to −75°) for that time period from our paleotopographic maps (Fig. 3A; see fig. S14 for an example). This distribution is split into 50 levels each with 2% probability. The simulations always start with zero ice sheet at all underlying land elevations. The mean surface temperature from the model at each latitudinal band is converted into the local surface temperature at each of the 50 elevation levels (each representing 2% of the latitudinal band) using a constant lapse rate of −6.5°C $km^{-1}$. At each latitude and each elevation level the thickness of the ice sheet is 0 if annual mean surface temperature at that elevation is above some maximum temperature for ice sheets to exist. The ice sheet thickness then increases linearly until it reaches present-day thickness if annual-mean temperature at that elevation drops to present-day levels at that latitude. When an ice sheet grows, the elevation of the surface increases and surface temperatures drop using the lapse rate.

The temperature above which ice sheets cannot exist is set to the minimum latitudinal- and annual-mean surface temperature in the present-day Southern Hemisphere where ice sheets do not exist (−8.4°C), where 1° latitudinal resolution is applied in the averaging. All temperatures for the present day are calculated from the ERA5 reanalysis from 2003–2023 (*83*) using 2m air temperature averaged over 1° latitude and as an annual-mean. Present-day elevations by latitude are calculated from are the GMTED2010 dataset (*84*).

How well does our EBM reproduce the high-latitude temperature response to changes in global mean temperature? Gaskell *et al*. (*8*) evaluate the latitudinal temperature gradient (LTG) over the past 90 Myr using paleodata, defining it as the difference between Southern Ocean sea-surface temperatures (south of 60°S) and low-latitude temperatures (±30°). They relate LTG to global mean sea-surface temperature and identify a near-linear relationship, with a slope of −0.66 ± 0.21 and an intercept of 36.53 ± 5.14°C. These data indicate that for each 1°C increase in global temperature, the equator-to-Southern Ocean temperature gradient decreases by 0.66 ± 0.21°C, providing a paleo-constraint on Southern Hemisphere polar amplification over the past 90 Myr. When forced with spatially uniform RF, our EBM reproduces a similarly near-linear LTG–global mean surface temperature relationship ($R^2$= 0.97), with a slope of −0.84 and an intercept of 39.85°C (fig. S15). These values fall within the uncertainty range reported by (*8*), indicating that the model faithfully captures the magnitude of Southern Hemisphere polar amplification. Notably, among the more complex Earth system models assessed by (*8*), none of the five Pliocene simulations reproduce the paleodata-constrained slope within the uncertainty range, and only one of six Eocene simulations (NorESM) is consistent with it; however, this model fails to match the constraint during the Pliocene (*8*). Given our focus on Antarctic cooling in response to global temperature decline, our EBM provides a robust and well-constrained framework for this analysis, with results shown in Fig. 5 and fig. S17 and described in the main text.

### Ice sheet representation

The model used here derives from that presented and made available by (*24*). Two new improvements have been made. First, the underlying relationship between benthic foraminiferal carbonate oxygen isotope ratio ($\delta^{18}O_c$) and ice-volume-related sea-level anomaly relative to the present ($z_{SL}$) is no longer simply the median regression based on Spratt and Lisiecki (*85*), as previously used in Rohling *et al*. (*6*, *24*, *86*). Instead, the current version employs the entire 95% range of the previous regression. Within that envelope, a wide variety of monotonic functions was fitted in a Monte Carlo style assessment (N= 500; no significant changes occur once N>100), to preserve long-term autocorrelation in the relationship between these two parameters while still allowing full variability across the uncertainty range of the regression (fig. S18). All iterations top out at $z_{SL}$ = 65.1 m, the value at which global ice-free conditions are reached. For each Monte Carlo iteration, the further

Downloaded from https://www.science.org at University of Southampton on October 15, 2026

ice-volume assessments are made, as in Rohling *et al.* (*6*, *24*, *86*). Finally, the findings are evaluated across all Monte Carlo iterations to determine the median and 2.5$^{th}$, 16$^{th}$, 84$^{th}$, and 97.5$^{th}$ percentiles (i.e., median, and the 68 and 95% probability envelopes). Reconstructed AIS volumes through time are shown in fig. S19.

Second, the current model version no longer assumes a constant ice sheet height over radius aspect ratio ($\varepsilon = h/r$). Instead, the model now includes dynamic ice-aspect ratios in response to two drivers:

• The first driver is the mean bed slope, which can be positive (higher center than margin) to negative (lower center than margin) due to: (i) initial topography after (*6*, *24*, *86*), which was based on (*87*); and (ii) cumulative glacio-isostatic adjustments that respond to ice-mass changes through time, using the calculations detailed in (*24*). The model calculates the response between bed slope and ice sheet aspect ratio in a linear manner.

• The second driver for change in the ice sheet aspect ratio is bed friction, which can be reduced by the presence of water and regolith [e.g., (*88*–*91*)]. The model accounts for this based on the growth or decay of ice volume. Under growth conditions, melt penetration to the ice bed is reduced and regolith is eroded, so friction increases and $\varepsilon$ increases; the ice profile becomes steeper. Under decay conditions, water penetration increases, and regolith can be re-established one ice-free conditions return, so friction decreases and $\varepsilon$ decreases; accordingly, the ice profile becomes flatter. These influences are approximated in a basic manner using an asymmetric function comprising a 0.3% ice sheet aspect-ratio decrease per 1-kyr time-step under decay conditions based on an order of a million-year timescale for regolith re-establishment following a climate change (*93*), and a 3% ice sheet aspect-ratio increase per 1-kyr time-step under growth conditions to approximate an order of magnitude more rapid removal of regolith due to active erosion by ice.

• The influences of the two drivers for $\varepsilon$ change are considered in sequence (first the friction effect, then the slope effect). Finally, a scaling of the results is applied so that the greatest considered for all ice sheets except the Greenland Ice Sheet (GrIS) is similar to the mean value for the modern Antarctic Ice Sheet ($\sim 2.15 \times 10^{-3}$). A multiplier of 2 is applied to the GrIS based on its modern dimensions (modern $\varepsilon_{GrIS} = \sim 4.5 \times 10^{-3}$); note that this choice for GrIS does not affect the entirely AIS-focused conclusions drawn here. The minimum $\varepsilon$ for all ice sheets is set at 0.5 times their maximum value [for consistency with sensitivity tests in (*6*, *86*)]. As an alternative, we have applied a $1/\sqrt{2}$ multiplier, following Eq. 5.7 of Benn and Evans (*93*); this does not materially change the conclusions drawn here. The inferred $\varepsilon$AIS values are shown in fig. S20.

Figure S21 shows inferred AIS summit altitude and bed elevation starting with an initial bed elevation of 1,270 m above sea level [after (*87*)]. Inferred AIS radius changes through time are shown in the main text (Fig. 1B). Figure S22 shows the percentage of Monte Carlo simulations in our probabilistic assessment for which Antarctic ice exists (i.e., AIS radius > 0 m). Changes in the aspect-ratio through time (fig. S20) cause relatively large radii for the early AIS, despite relatively small volumes (fig. S19); in other words, the early AIS was relatively flat and spatially extensive.

## REFERENCES AND NOTES


1. M. Morlighem *et al.*, Deep glacial troughs and stabilizing ridges unveiled beneath the margins of the Antarctic ice sheet. *Nat. Geosci.* **13**, 132–137 (2020). doi: 10.1038/s41561-019-0510-8
2. C. R. Stokes *et al.*, Response of the East Antarctic Ice Sheet to past and future climate change. *Nature* **608**, 275–286 (2022). doi: 10.1038/s41586-022-04946-0; pmid: 35948707
3. T. Westerhold *et al.*, An astronomically dated record of Earth's climate and its predictability over the last 66 million years. *Science* **369**, 1383–1387 (2020). doi: 10.1126/science.aba6853; pmid: 32913105
4. R. M. DeConto, D. Pollard, Rapid Cenozoic glaciation of Antarctica induced by declining atmospheric $CO_2$. *Nature* **421**, 245–249 (2003). doi: 10.1038/nature01290; pmid: 12529638
5. S. Galeotti *et al.*, Antarctic Ice Sheet variability across the Eocene-Oligocene boundary climate transition. *Science* **352**, 76–80 (2016). doi: 10.1126/science.aab0669; pmid: 27034370
6. E. J. Rohling *et al.*, Comparison and synthesis of sea-level and deep-sea temperature variations over the past 40 million years. *Rev. Geophys.* **60**, e2022RG000775 (2022).
7. C. L. O'Brien *et al.*, The enigma of Oligocene climate and global surface temperature evolution. *Proc. Natl. Acad. Sci. U.S.A.* **117**, 25302–25309 (2020). doi: 10.1073/pnas.2003914117; pmid: 32989142
8. D. E. Gaskell *et al.*, The latitudinal temperature gradient and its climate dependence as inferred from foraminiferal $\delta^{18}O$ over the past 95 million years. *Proc. Natl. Acad. Sci. U.S.A.* **119**, e2111332119 (2022). doi: 10.1073/pnas.2111332119; pmid: 35254906
9. M. E. Raymo, W. F. Ruddiman, Tectonic forcing of late Cenozoic climate. *Nature* **359**, 117–122 (1992). doi: 10.1038/359117a0
10. A. S. Merdith *et al.*, Phanerozoic icehouse climates as the result of multiple solid-Earth cooling mechanisms. *Sci. Adv.* **11**, eadm9798 (2025). doi: 10.1126/sciadv.adm9798; pmid: 39951538
11. V. R. Barletta *et al.*, Observed rapid bedrock uplift in Amundsen Sea Embayment promotes ice-sheet stability. *Science* **360**, 1335–1339 (2018). doi: 10.1126/science.aao1447; pmid: 29930133
12. E. Gasson, R. DeConto, D. Pollard, Antarctic bedrock topography uncertainty and ice sheet stability. *Geophys. Res. Lett.* **42**, 5372–5377 (2015). doi: 10.1002/2015GL064322
13. J. P. Klages *et al.*, Ice sheet-free West Antarctica during peak early Oligocene glaciation. *Science* **385**, 322–327 (2024). doi: 10.1126/science.adj3931; pmid: 38963876
14. I. D. Barr *et al.*, 60 million years of glaciation in the Transantarctic Mountains. *Nat. Commun.* **13**, 5526 (2022). doi: 10.1038/s41467-022-33310-z; pmid: 36130952
15. T. M. Gernon *et al.*, Rift-induced disruption of cratonic keels drives kimberlite volcanism. *Nature* **620**, 344–350 (2023). doi: 10.1038/s41586-023-06193-3; pmid: 37495695
16. T. M. Gernon *et al.*, Coevolution of craton margins and interiors during continental break-up. *Nature* **632**, 327–335 (2024). doi: 10.1038/s41586-024-07717-1; pmid: 39112622
17. D. H. A. Vermeulen, M. L. J. Baatsen, A. S. von der Heydt, Sustainability of regional Antarctic ice sheets under late Eocene seasonal atmospheric conditions. *Clim. Past* **21**, 95–114 (2025). doi: 10.5194/cp-21-95-2025
18. G. J. G. Paxman *et al.*, Reconstructions of Antarctic topography since the Eocene–Oligocene boundary. *Palaeogeogr. Palaeoclimatol. Palaeoecol.* **535**, 109346 (2019). doi: 10.1016/j.palaeo.2019.109346
19. S. Brune, S. E. Williams, N. P. Butterworth, R. D. Müller, Abrupt plate accelerations shape rifted continental margins. *Nature* **536**, 201–204 (2016). doi: 10.1038/nature18319; pmid: 27437571
20. S. Bo *et al.*, The Gamburtsev mountains and the origin and early evolution of the Antarctic Ice Sheet. *Nature* **459**, 690–693 (2009). doi: 10.1038/nature08024; pmid: 19494912
21. G. J. G. Paxman *et al.*, Erosion-driven uplift in the Gamburtsev Subglacial Mountains of East Antarctica. *Earth Planet. Sci. Lett.* **452**, 1–14 (2016). doi: 10.1016/j.epsl.2016.07.040
22. K. C. Rose *et al.*, Early East Antarctic Ice Sheet growth recorded in the landscape of the Gamburtsev Subglacial Mountains. *Earth Planet. Sci. Lett.* **375**, 1–12 (2013). doi: 10.1016/j.epsl.2013.03.053
23. E. J. Lea, S. S. R. Jamieson, M. J. Bentley, Alpine topography of the Gamburtsev Subglacial Mountains, Antarctica, mapped from ice sheet surface morphology. *Cryosphere* **18**, 1733–1751 (2024). doi: 10.5194/tc-18-1733-2024
24. E. J. Rohling *et al.*, Reconciling the apparent discrepancy between Cenozoic deep-sea temperatures from proxies and from benthic oxygen isotope deconvolution. *Paleoceanogr. Paleoclimatol.* **39**, e2024PA004872 (2024).
25. A. Tripati, J. Backman, H. Elderfield, P. Ferretti, Eocene bipolar glaciation associated with global carbon cycle changes. *Nature* **436**, 341–346 (2005). doi: 10.1038/nature03874; pmid: 16034408
26. J. B. Anderson *et al.*, Progressive Cenozoic cooling and the demise of Antarctica's last refugium. *Proc. Natl. Acad. Sci. U.S.A.* **108**, 11356–11360 (2011). doi: 10.1073/pnas.1014885108; pmid: 21709269
27. J. Van Breedam, P. Huybrechts, M. Crucifix, Modelling evidence for late Eocene Antarctic glaciations. *Earth Planet. Sci. Lett.* **586**, 117532 (2022). doi: 10.1016/j.epsl.2022.117532
28. J. Braun, S. D. Willett, A very efficient O(n), implicit and parallel method to solve the stream power equation governing fluvial incision and landscape evolution. *Geomorphology* **180-181**, 170–179 (2013). doi: 10.1016/j.geomorph.2012.10.008
29. F. Ferraccioli *et al.*, East Antarctic rifting triggers uplift of the Gamburtsev Mountains. *Nature* **479**, 388–392 (2011). doi: 10.1038/nature10566; pmid: 22094700
30. C. J. Tochilin *et al.*, Erosional history of the Prydz Bay sector of East Antarctica from detrital apatite and zircon geo- and thermochronology multidating. *Geochem. Geophys. Geosyst.* **13**, 2012GC004364 (2012). doi: 10.1029/2012GC004364
31. K. Hochmuth *et al.*, The evolving paleobathymetry of the Circum-Antarctic Southern Ocean Since 34 Ma: A key to understanding past cryosphere-ocean developments. *Geochem. Geophys. Geosyst.* **21**, e2020GC009122 (2020).
32. H. Sirevaag, J. Jacobs, A. K. Ksienzyk, Substantial spatial variation in glacial erosion rates in the Dronning Maud Land Mountains, East Antarctica. *Commun. Earth Environ.* **2**, 244 (2021). doi: 10.1038/s43247-021-00315-3


Downloaded from https://www.science.org at University of Southampton on October 15, 2026

33. J. C. Hammond, F. A. Saavedra, S. K. Kampf, Global snow zone maps and trends in snow persistence 2001–2016. *Int. J. Climatol.* **38**, 4369–4383 (2018). doi: 10.1002/joc.5674
34. M. Zundel *et al.*, A large-scale transcontinental river system crossed West Antarctica during the Eocene. *Sci. Adv.* **10**, eadn6056 (2024). doi: 10.1126/sciadv.adn6056; pmid: 38838149
35. P. G. Fitzgerald, A. J. W. Gleadow, Fission-track geochronology, tectonics and structure of the Transantarctic Mountains in Northern Victoria land, Antarctica. *Chem. Geol. Isot. Geosci. Sect.* **73**, 169–198 (1988). doi: 10.1016/0168-9622(88)90014-0
36. S. R. Miller, P. G. Fitzgerald, S. L. Baldwin, Cenozoic range-front faulting and development of the Transantarctic Mountains near Cape Surprise, Antarctica: Thermochronologic and geomorphologic constraints. *Tectonics* **29**, TC1003 (2010). doi: 10.1029/2009TC002457
37. J. W. Goodge, Geological and tectonic evolution of the Transantarctic Mountains, from ancient craton to recent enigma. *Gondwana Res.* **80**, 50–122 (2020). doi: 10.1016/j.gr.2019.11.001
38. W. Shen *et al.*, Seismic evidence for lithospheric foundering beneath the southern Transantarctic Mountains, Antarctica. *Geology* **46**, 71–74 (2017). doi: 10.1130/G39555.1
39. T. A. Jordan, T. R. Riley, C. S. Siddoway, The geological history and evolution of West Antarctica. *Nat. Rev. Earth Environ.* **1**, 117–133 (2020). doi: 10.1038/s43017-019-0013-6
40. R. Winkelmann *et al.*, The Potsdam Parallel Ice Sheet Model (PISM-PIK) – Part 1: Model description. *Cryosphere* **5**, 715–726 (2011). doi: 10.5194/tc-5-715-2011
41. J. A. N. Hazzard, F. D. Richards, Antarctic geothermal heat flow, crustal conductivity and heat production inferred from seismological data. *Geophys. Res. Lett.* **51**, e2023GL106274 (2024).
42. P. J. Valdes, C. R. Scotese, D. J. Lunt, Deep ocean temperatures through time. *Clim. Past* **17**, 1483–1506 (2021). doi: 10.5194/cp-17-1483-2021
43. B. Parazin *et al.*, Ice sheets without dynamic topography. *Geophys. Res. Lett.* **52**, e2025GL115332 (2025).
44. E. J. Judd *et al.*, A 485-million-year history of Earth's surface temperature. *Science* **385**, eadk3705 (2024). doi: 10.1126/science.adk3705; pmid: 39298603
45. T. E. van Peer *et al.*, Eccentricity pacing and rapid termination of the early Antarctic ice ages. *Nat. Commun.* **15**, 10600 (2024). doi: 10.1038/s41467-024-54186-1; pmid: 39639043
46. P. Goodwin, R. G. Williams, P. Ceppi, B. B. Cael, Climate feedbacks derived from spatial gradients in recent climatology. *J. Geophys. Res. Atmos.* **130**, e2024JD043186 (2025). doi: 10.1029/2024JD043186
47. P. Goodwin, R. G. Williams, On the Arctic amplification of surface warming in a conceptual climate model. *Physica D* **454**, 133880 (2023). doi: 10.1016/j.physd.2023.133880
48. C. R. Scotese, H. Song, B. J. W. Mills, D. G. van der Meer, Phanerozoic paleotemperatures: The earth's changing climate during the last 540 million years. *Earth Sci. Rev.* **215**, 103503 (2021). doi: 10.1016/j.earscirev.2021.103503
49. P. R. Bierman, J. D. Shakun, L. B. Corbett, S. R. Zimmerman, D. H. Rood, A persistent and dynamic East Greenland Ice Sheet over the past 7.5 million years. *Nature* **540**, 256–260 (2016). doi: 10.1038/nature20147; pmid: 27929005
50. A. Bufe, J. K. C. Rugenstein, N. Hovius, $CO_2$ drawdown from weathering is maximized at moderate erosion rates. *Science* **383**, 1075–1080 (2024). doi: 10.1126/science.adk0957; pmid: 38452079
51. J. R. Zondervan *et al.*, Rock organic carbon oxidation $CO_2$ release offsets silicate weathering sink. *Nature* **623**, 329–333 (2023). doi: 10.1038/s41586-023-06581-9; pmid: 37794192
52. P. F. Barker, G. M. Filippelli, F. Florindo, E. E. Martin, H. D. Scher, Onset and role of the Antarctic Circumpolar Current. *Deep Sea Res. Part II Top. Stud. Oceanogr.* **54**, 2388–2398 (2007). doi: 10.1016/j.dsr2.2007.07.028
53. F. S. Hoem *et al.*, Strength and variability of the Oligocene Southern Ocean surface temperature gradient. *Commun. Earth Environ.* **3**, 322 (2022). doi: 10.1038/s43247-022-00666-5
54. I. Sauermilch *et al.*, Gateway-driven weakening of ocean gyres leads to Southern Ocean cooling. *Nat. Commun.* **12**, 6465 (2021). doi: 10.1038/s41467-021-26658-1; pmid: 34753912
55. B. Bovy, R. Lange, fastscape-lem/fastscape: Release v0.1.0, Zenodo (2023); https://doi.org/10.5281/zenodo.3479425.
56. B. Bovy, J. Braun, A. Glerum, S. Wolf, fastscape-lem/fastscapelib-fortran: Release v2.8, Zenodo (2023); https://doi.org/10.5281/zenodo.2553407.
57. T. van de Flierdt, S. R. Hemming, S. L. Goldstein, G. E. Gehrels, S. E. Cox, Evidence against a young volcanic origin of the Gamburtsev Subglacial Mountains, Antarctica. *Geophys. Res. Lett.* **35**, L21303 (2008). doi: 10.1029/2008GL035564
58. J. J. Veevers, Case for the Gamburtsev Subglacial Mountains of East Antarctica originating by mid-Carboniferous shortening of an intracratonic basin. *Geology* **22**, 593 (1994). doi: 10.1130/0091-7613(1994)022<0593:CFTGSM>2.3.CO;2
59. I. M. Artemieva, L. P. Vinnik, Density structure of the cratonic mantle in southern Africa: 1. Implications for dynamic topography. *Gondwana Res.* **39**, 204–216 (2016). doi: 10.1016/j.gr.2016.03.002
60. M. An *et al.*, Temperature, lithosphere-asthenosphere boundary, and heat flux beneath the Antarctic Plate inferred from seismic velocities. *J. Geophys. Res. Solid Earth* **120**, 8720–8742 (2015). doi: 10.1002/2015JB011917
61. T. M. Gernon *et al.*, Enriched mantle generated through persistent convective erosion of continental roots. *Nat. Geosci.* **18**, 1311–1318 (2025). doi: 10.1038/s41561-025-01843-9
62. C. J. Swain, J. F. Kirby, Effective elastic thickness map reveals subglacial structure of East Antarctica. *Geophys. Res. Lett.* **48**, e2020GL091576 (2021).
63. S. S. Sandha, M. Aggarwal, I. Fedorov, M. Srivastava, "Mango: A Python Library for Parallel Hyperparameter Tuning," ICASSP 2020 - 2020 IEEE International Conference on Acoustics, Speech and Signal Processing (ICASSP), Barcelona, Spain, 4 to 8 May 2020. (IEEE, 2020), pp. 3987–3991.
64. D. McKenzie, The influence of dynamically supported topography on estimates of Te. *Earth Planet. Sci. Lett.* **295**, 127–138 (2010). doi: 10.1016/j.epsl.2010.03.033
65. J. Braun, Pecube: A new finite-element code to solve the 3D heat transport equation including the effects of a time-varying, finite amplitude surface topography. *Comput. Geosci.* **29**, 787–794 (2003). doi: 10.1016/S0098-3004(03)00052-9
66. P. G. Fitzgerald, Thermochronologic constraints on post-Paleozoic tectonic evolution of the central Transantarctic Mountains, Antarctica. *Tectonics* **13**, 818–836 (1994). doi: 10.1029/94TC00595
67. S. N. Thomson, P. W. Reiners, S. R. Hemming, G. E. Gehrels, The contribution of glacial erosion to shaping the hidden landscape of East Antarctica. *Nat. Geosci.* **6**, 203–207 (2013). doi: 10.1038/ngeo1722
68. T. Salles *et al.*, Hundred million years of landscape dynamics from catchment to global scale. *Science* **379**, 918–923 (2023). doi: 10.1126/science.add2541; pmid: 36862774
69. M. Chang, S. S. R. Jamieson, M. J. Bentley, C. R. Stokes, The surficial and subglacial geomorphology of western Dronning Maud Land, Antarctica. *J. Maps* **12**, 892–903 (2016). doi: 10.1080/17445647.2015.1097289
70. H. Sirevaag, A. K. Ksienzyk, J. Jacobs, I. Dunkl, A. Läufer, Tectono-thermal evolution and morphodynamics of the Central Dronning Maud Land Mountains, East Antarctica, based on new thermochronological data. *Geosciences (Basel)* **8**, 390 (2018). doi: 10.3390/geosciences8110390
71. H. K. Coxall, P. A. Wilson, H. Pälike, C. H. Lear, J. Backman, Rapid stepwise onset of Antarctic glaciation and deeper calcite compensation in the Pacific Ocean. *Nature* **433**, 53–57 (2005). doi: 10.1038/nature03135; pmid: 15635407
72. E. Gasson, R. M. DeConto, D. Pollard, R. H. Levy, Dynamic Antarctic ice sheet during the early to mid-Miocene. *Proc. Natl. Acad. Sci. U.S.A.* **113**, 3459–3464 (2016). doi: 10.1073/pnas.1516130113; pmid: 26903645
73. G. J. G. Paxman, E. G. W. Gasson, S. S. R. Jamieson, M. J. Bentley, F. Ferraccioli, Longterm increase in Antarctic ice sheet vulnerability driven by bed topography evolution. *Geophys. Res. Lett.* **47**, e2020GL090003 (2020).
74. G. J. G. Paxman, S. S. R. Jamieson, A. M. Dolan, M. J. Bentley, Subglacial valleys preserved in the highlands of south and east Greenland record restricted ice extent during past warmer climates. *Cryosphere* **18**, 1467–1493 (2024). doi: 10.5194/tc-18-1467-2024
75. D. R. Greenwood, S. L. Wing, Eocene continental climates and latitudinal temperature gradients. *Geology* **23**, 1044 (1995). doi: 10.1130/0091-7613(1995)023<1044:ECCALT>2.3.CO;2
76. J. Pross *et al.*, Persistent near-tropical warmth on the Antarctic continent during the early Eocene epoch. *Nature* **488**, 73–77 (2012). doi: 10.1038/nature11300; pmid: 22859204
77. L. Zhang, W. W. Hay, C. Wang, X. Gu, The evolution of latitudinal temperature gradients from the latest Cretaceous through the Present. *Earth Sci. Rev.* **189**, 147–158 (2019). doi: 10.1016/j.earscirev.2019.01.025
78. L. Nicola, D. Notz, R. Winkelmann, Revisiting temperature sensitivity: How does Antarctic precipitation change with temperature? *Cryosphere* **17**, 2563–2583 (2023). doi: 10.5194/tc-17-2563-2023
79. R. D. McCulloch *et al.*, Climatic inferences from glacial and palaeoecological evidence at the last glacial termination, southern South America. *J. Quaternary Sci.* **15**, 409–417 (2000). doi: 10.1002/1099-1417(200005)15:4<409:AID-JQS539>3.0.CO;2-%23
80. V. Montade, O. Peyron, C. Favier, J. P. Francois, S. G. Haberle, A pollen–climate calibration from western Patagonia for palaeoclimatic reconstructions. *J. Quaternary Sci.* **34**, 76–86 (2019). doi: 10.1002/jqs.3082
81. M. Baatsen, P. Bijl, A. von der Heydt, A. Sluijs, H. Dijkstra, Resilient Antarctic monsoonal climate prevented ice growth during the Eocene. *Clim. Past* **20**, 77–90 (2024). doi: 10.5194/cp-20-77-2024
82. G. J. G. Paxman, F. J. Clubb, S. S. R. Jamieson, A. L. Densmore, Valley longitudinal profiles record the fluvial landscape evolution and geological structure of the Gamburtsev Subglacial Mountains, East Antarctica. *EGUsphere* **2026**, 1 (2026). doi: 10.5194/egusphere-2026-847.
83. Copernicus Climate Change Service, ERA5 monthly averaged data on single levels from 1940 to present, Copernicus Climate Change Service (C3S) Climate Data Store (CDS, 2023); https://doi.org/10.24381/cds.f17050d7.
84. J. J. Danielson, D. B. Gesch, Global multi-resolution terrain elevation data 2010 (GMTED2010), U.S. Geological Survery Open-File Report 2011–1073 (USGS, 2011).
85. R. M. Spratt, L. E. Lisiecki, A Late Pleistocene sea level stack. *Clim. Past* **12**, 1079–1092 (2016). doi: 10.5194/cp-12-1079-2016


Downloaded from https://www.science.org at University of Southampton on October 15, 2026

86. E. J. Rohling *et al.*, Sea level and deep-sea temperature reconstructions suggest quasi-stable states and critical transitions over the past 40 million years. *Sci. Adv.* **7**, eabf5326 (2021). doi: 10.1126/sciadv.abf5326; pmid: 34172440
87. B. De Boer, R. S. W. van de Wal, R. Bintanja, L. J. Lourens, E. Tuenter, Cenozoic global ice-volume and temperature simulations with 1-D ice-sheet models forced by benthic $\delta^{18}O$ records. *Ann. Glaciol.* **51**, 23–33 (2010). doi: 10.3189/172756410791392736
88. P. U. Clark, D. Pollard, Origin of the Middle Pleistocene Transition by ice sheet erosion of regolith. *Paleoceanography* **13**, 1–9 (1998). doi: 10.1029/97PA02660
89. A. Ganopolski, R. Calov, The role of orbital forcing, carbon dioxide and regolith in 100 kyr glacial cycles. *Clim. Past* **7**, 1415–1425 (2011). doi: 10.5194/cp-7-1415-2011
90. C. R. Tabor, C. J. Poulsen, Simulating the mid-Pleistocene transition through regolith removal. *Earth Planet. Sci. Lett.* **434**, 231–240 (2016). doi: 10.1016/j.epsl.2015.11.034
91. M. Willeit, A. Ganopolski, R. Calov, V. Brovkin, Mid-Pleistocene transition in glacial cycles explained by declining $CO_2$ and regolith removal. *Sci. Adv.* **5**, eaav7337 (2019). doi: 10.1126/sciadv.aav7337; pmid: 30949580
92. J. Braun, J. Mercier, F. Guillocheau, C. Robin, A simple model for regolith formation by chemical weathering. *J. Geophys. Res. Earth Surf.* **121**, 2140–2171 (2016). doi: 10.1002/2016JF003914
93. D. Benn, D. Evans, *Glaciers and Glaciation* (Hodder Education, 2010).
94. T. K. Hincks, T. M. Gernon, G. J. G. Paxman, Supplementary data files for landscape and ice sheet modelling - Gernon et al., 2026, Continental breakup-driven uplift instigated East Antarctic Ice Sheet formation, Zenodo (2026); https://doi.org/10.5281/zenodo.19205651.
95. WASP Earth System Model, Wasp-esm/energy balance model: Energy balance model, Zenodo (2023); https://doi.org/10.5281/zenodo.8151916.
96. P. Goodwin, Code for: Continental breakup-driven uplift instigated East Antarctic Ice Sheet formation (2026), Zenodo (2026); https://doi.org/10.5281/zenodo.20758885.
97. E. Rohling, T. M. Gernon, A Probabilistic Ice-Sheet Parameterization for Antarctic Ice-Sheet Evolution, Dryad (2026); https://doi.org/10.5061/dryad.sbcc2frkt.
98. B. Hönisch *et al.*, Toward a Cenozoic history of atmospheric $CO_2$. *Science* **382**, eadi5177 (2023). doi: 10.1126/science.adi5177; pmid: 38060645
99. C. R. Scotese, An atlas of Phanerozoic paleogeographic maps: The seas come in and the seas go out. *Annu. Rev. Earth Planet. Sci.* **49**, 679–728 (2021). doi: 10.1146/annurev-earth-081320-064052
100. T. M. Gernon *et al.*, Global chemical weathering dominated by continental arcs since the mid-Palaeozoic. *Nat. Geosci.* **14**, 690–696 (2021). doi: 10.1038/s41561-021-00806-0



## ACKNOWLEDGMENTS

We gratefully acknowledge long-term support (to T.M.G.) from the WoodNext Foundation, a fund of a donor-advised fund program, which made this study possible. We acknowledge the developers of the open-source software used in this study, including Fastscape (fastscape.org) and PISM (pism.io), which made our analyses possible. We thank the anonymous reviewers for their constructive comments that greatly improved the paper. We also thank B. Steinberger for helpful discussions on dynamic topography in Antarctica. We are grateful to H. Sirevaag for providing published thermochronological age data from the Dronning Maud Land region of Antarctica. The illustrations shown in Fig. 1C are by G. Hincks. The photograph of the Dronning Maud Land Mountains (Fig. 2A) is by W. Bauer, used under a Creative Commons Attribution-ShareAlike 3.0 license (CC BY-SA 3.0). **Funding:** T.M.G. and T.K.H. are funded by the WoodNext Foundation, a fund of a donor-advised fund program. G.J.G.P. is funded by a Royal Society University Research Fellowship (award number URF\R1\241308). S.B. is funded by the European Research Council (ERC) (EMERGE; award number 101087245). **Author contributions:** Conceptualization and project administration: T.M.G.; Funding acquisition: T.M.G.; Interpretation: T.G., T.K.H., P.G., G.J.G.P., S.B.; Geodynamic interpretation: T.M.G., S.B., D.K.; Methodology and data curation: T.M.G., T.K.H., P.G., G.J.G.P., S.B., E.J.R., J.B.; Landscape evolution analysis: T.K.H., T.M.G., J.B.; PISM ice sheet modeling: G.J.G.P.; Energy balance modeling: P.G., T.K.H., T.M.G.; Ice sheet parameterization: E.J.R.; Visualization: T.K.H., T.M.G., G.J.P.G., E.J.R.; Writing – original draft: T.M.G., T.K.H., G.J.G.P., P.G.,. E.J.R.; Writing – review & editing: All authors. **Competing interests:** The authors declare that they have no competing interests. **Data, code, and materials availability:** The FastScape landscape evolution model is openly available at https://github.com/fastscape-lem/fastscape, with documentation at https://fastscape.readthedocs.io/en/latest/. All model input parameters, including those used in the uncertainty analysis, are provided in tables S1 to S3. Model outputs (including Geographic Information System datasets) and additional supplementary files are archived on Zenodo (*94*). The PISM is openly available at https://www.pism.io/. Scripts and input files are also archived on Zenodo (*94*). Additional information on the energy balance model, updated from (*95*), is available on Zenodo (*96*). Data files and R scripts required to reproduce the ice sheet parameterization are available on Dryad (*97*). No new materials were generated in this study.

**License information:** Copyright © 2026 the authors, some rights reserved; exclusive licensee American Association for the Advancement of Science. No claim to original US government works. https://www.science.org/about/science-licenses-journal-article-reuse.
This research was funded in part by the European Research Council (EMERGE; award number 101087245); as required, the author will make the Author Accepted Manuscript (AAM) version available under a CC BY public copyright license.

## SUPPLEMENTARY MATERIALS

science.org/doi/10.1126/science.adz6758
Supplementary Text; Figs. S1 to S22; Tables S1 to S5; ; References (*101–119*); Movies S1 and S2

Submitted 5 September 2025; accepted 22 April 2026

10.1126/science.adz6758

**Corrected (9 July 2026):** Prior to publication, reference renumbering occurred, but a few instances where renumbering was required in Fig. 1 and its legend were missed. These have been corrected. Reference renumbering errors have also been addressed in the supplementary materials. Additionally, a URL error in the data, code, and materials availability section of the acknowledgements has been corrected.

Downloaded from https://www.science.org at University of Southampton on October 15, 2026

# Continental breakup–driven uplift instigated East Antarctic Ice Sheet formation

Thomas M. Gernon, Thea K. Hincks, Philip Goodwin, Guy J. G. Paxman, Sascha Brune, Eelco J. Rohling, Derek Keir, and Jean Braun

*Science* **393** (6806), eadz6758. DOI: 10.1126/science.adz6758

**Editor's summary**

What factors led to the initiation of glaciation in Antarctica some 34 million years ago? Declining concentrations of atmospheric carbon dioxide is considered the primary reason, but other mechanisms were probably also important. Gernon *et al*. investigated the role of regional topographic uplift caused by Jurassic continental breakup and subsequent mantle surface feedbacks. They found that growth of the East Antarctica plateau and the Eocene uplift of the Gamburtsev Mountains pushed landscapes past the threshold for ice sheet nucleation about 45 million years ago, overcoming what would otherwise have been prohibitively warm temperatures. —Jesse Smith

**View the article online**

https://www.science.org/doi/10.1126/science.adz6758

**Permissions**

https://www.science.org/help/reprints-and-permissions

Downloaded from https://www.science.org at University of Southampton on October 15, 2026

Use of this article is subject to the Terms of service

*Science* (ISSN 1095-9203) is published by the American Association for the Advancement of Science. 1200 New York Avenue NW, Washington, DC 20005. The title *Science* is a registered trademark of AAAS.

Copyright © 2026 The Authors, some rights reserved; exclusive licensee American Association for the Advancement of Science. No claim to original U.S. Government Works